TISSUE IMAGING WITH SCANNING ACOUSTIC MICROSCOPY AND RAMAN SPECTROSCOPY

by

Melita Parlak

B.S., Physics, Boğaziçi University, 2017

Submitted to the Institute for Graduate Studies in
Science and Engineering in partial fulfillment of
the requirements for the degree of
Master of Science

Graduate Program in Physics

Boğaziçi University

2020

ACKNOWLEDGEMENTS

I would like to express my gratitude to my advisor, Prof. Burçin Ünlü, for giving me this opportunity to work in such a fantastic environment. He has always been there with his support and supervision throughout this work.

I would also like to express my sincere thanks to Assoc. Prof. Özgür Özdemir and Assist. Prof. Hakan Erkol for participating in my thesis committee.

I want to thank all members of the Medical and Biological Physics Laboratory for providing me with a warm and encouraging atmosphere to work. Special thanks to Bükem Tanören, Natali Sözüdoğru, Uğur Parlatan, and İrem Demirkan.

I also would like to acknowledge the funding support that made my graduate research possible. I was funded by TUBITAK (Project No: 117F407), scanning acoustic microscopy and Raman spectroscopy studies were supported by the Ministry of Development of Turkey (Project Number: 2009K120520).

I would like to thank all my friends who believed in me and respected this work, especially to Doğan Macit for giving constant support on such crucial times, to Adalet Eroğlu and for her never-ending trust and to Suat Dönertaş for his support.

Most importantly, I am more than grateful to my family for their endless confidence in me, which encouraged me many times to pick myself back up again and keep doing my best. I would not be able to finish this work without their support.

ABSTRACT

TISSUE IMAGING WITH SCANNING ACOUSTIC MICROSCOPY AND RAMAN SPECTROSCOPY

The morphological and mechanical characteristics of tissues are critical in biology and medicine. Furthermore, external agents might cause various modifications in the biological samples that alter the physiological properties. Thus, studying the mechanical and optical properties of tissue is vital in the theranostic processes of the diseases. For characterizing the acousto-mechanical properties of biological samples, scanning acoustic microscopy (SAM) is introduced as an imaging method. We used the colloidal semiconductor quantum dots (QD's) as contrast agents for SAM. Since QD's aggregation is significant, especially in targeted nanoparticle-based drug delivery systems, the acoustic impedance values of aggregated QD were measured with SAM. It turns out that the acoustic impedance values are proportional to the volume and the heterogeneity of aggregation. Also, we studied liver tissues of rats exposed to phthalates, which were applied to modify the flexibility. Therefore, the mechanical properties of tissues varied. Apart from SAM, Raman spectroscopy is another sensing tool that uses light to characterize the tissue. Raman spectrum provides molecular information since the peaks in the spectra represent the vibrational transition energies of the chemical bonds in the sample. In this thesis, we also investigated the Raman spectra (RS) of rat liver tissues that were exposed to phthalate and the ones that were not exposed. We showed that DNA, protein, and the lipid/collagen structure changed due to exposure to phthalate esters. As a result, this thesis revealed that SAM and RS techniques could determine and confirm mechano-chemical alterations of the biological samples.

ÖZET

TARAMALI AKUSTİK MİKROSKOP VE RAMAN SPEKTROMETRİ İLE DOKU GÖRÜNTÜLEMESİ

Dokuların morfolojik ve mekanik özellikleri biyoloji ve tıpta önemlidir. Dahası, harici maddeler biyolojik numunelerde fizyolojik özellikleri değiştiren çeşitli modifikasyonlara neden olabilir. Bu nedenle, dokunun mekanik ve optik özelliklerinin incelenmesi, hastalıkların terapötik süreçlerinde hayati önem taşır. Biyolojik numunelerin akustik-mekanik özelliklerini karakterize etmek için, bir görüntüleme yöntemi olarak taramalı akustik mikroskopi (TAM) tanıtıldı. Kolloidal yarı iletken kuantum noktaları (KN'lar) TAM için kontrast ajanları olarak araştırdık. KN'ların toplanması, özellikle hedeflenen nanopartikül bazlı ilaç verme sistemlerinde önemli olduğundan, kümelenmiş KN'ların akustik empedans değerleri TAM ile ölçtük. Akustik empedans değerlerinin kümelenmelerin hacimleri ve heterojenliği ile orantılı olduğunu gösterdik. Ayrıca, esnekliği değiştirmek için uygulanan ftalatlara maruz kalan farelerin karaciğer dokularındaki değişiklikleri inceledik. Akustik mikroskop dışında, Raman spektroskopisi dokuyu karakterize etmek için kullanan başka bir metottur. Raman spektrumu, spektrumdaki tepeler numunedeki kimyasal bağların titreşim enerjilerini temsil ettiği için moleküler bilgi sağlar. Bu tezde, ftalata maruz bırakılan veya bırakılmayan farelerin karaciğer dokularının Raman spektrumlarını da araştırdık. Ftalat esterlerine maruz kalmaya bağlı olarak DNA, protein ve lipid / kolajen yapısının değiştiğini gösterdik. Sonuç olarak, bu tez, akustik mikroskop ve Raman spektrometre tekniklerinin biyolojik numunelerin mekanik-kimyasal değişikliklerini belirleyebileceğini ve doğrulayabileceğini ortaya koydu.

TABLE OF CONTENTS

LIST OF FIGURES

LIST OF TABLES

LIST OF SYMBOLS

a	Scatterer source size
A	Absorption
α	Polarizability
α_0	Polarizability at the equilibrium
A_i	Amplitude of incident pressure wave
A_t	Amplitude of transmitted pressure wave
A_r	Amplitude of reflected pressure wave
A_{shear}	Amplitude of incident shear wave
A_{st}	Amplitude of transmitted shear wave
A_{sr}	Amplitude of reflected shear wave
$\mathbf{E}$	Electric field
E_0	Amplitude of electric field
E	Energy
E_1	Energy of the first state
E_2	Energy of the second state
ΔE	Energy difference
c	Sound speed
υ_1	Particle velocity in medium-1
υ_2	Particle velocity in medium-2
$\mathbf{k}$	Wave number
k_1	Wave number in medium-1
k_{L1}	Wave number in liquid medium
k_{S1}	Wave number in solid medium
k_2	Wave number in medium-2
λ	Wavelength
ν	Frequency
ν_0	Frequency of incident photon
ν_m	Frequency of vibration

$\bar{\nu}$	Wavenumber
h	Planck constant
ψ	Plane wave
ψ_i	Incident plane wave
ψ_r	Reflected plane wave
ψ_t	Transmitted plane wave
ψ_{si}	Incident shear wave
ψ_{sr}	Reflected shear wave
ψ_{st}	Transmitted shear wave
κ	Compressibility
ρ	Density of the surrounding
ρ_1	Density of the medium-1
ρ_2	Density of the medium-2
ω	Angular frequency
$\mathbf{r}$	Direction of the wave propagation
$p(\mathbf{r}, t)$	Acoustic wave pressure
m	Mass
P	Dipole moment
R	Reflection coefficient
T	Transmission coefficient
t	time
υ_i	Incident wave velocity
υ_t	Transmitted wave velocity
υ_r	Reflected wave velocity
θ_i	Angle of incident wave
θ_t	Angle of transmitted wave
θ_r	Angle of reflected wave
θ_{si}	Angle of incident shear wave
θ_{st}	Angle of transmitted shear wave
θ_{sr}	Angle of reflected shear wave
$S_{Reference}$	Signal of reference

S_0	Generated signal
Z	Acoustic impedance
Z_1	Acoustic impedance of medium-1
Z_2	Acoustic impedance of medium-2
$Z_{Reference}$	Acoustic impedance of reference
Z_{Sample}	Acoustic impedance of sample
$Z_{Substrate}$	Acoustic impedance of substrate

LIST OF ACRONYMS/ABBREVIATIONS

1D	One Dimensional
2D	Two Dimensional
3D	Three Dimensional
AI	Acoustic Impedance
CT	Computed Tomography
CdTe/CdS	Cadmium Telluride/Cadmium Sulphide
fMRI	Functional Magnetic Resonance Imaging
GQD	Graphene Quantum Dot
GHz	Gigahertz
MRI	Magnetic Resonance Imaging
MHz	Megahertz
PET	Positron Emission Tomography
SAM	Scanning Acoustic Microscopy
SOS	Speed of Sound
PbS	Lead Sulfide
RS	Raman Spectroscopy
QD	Quantum Dot

1. INTRODUCTION

In the late 19 century, medical imaging has begun with the unexpected discovery of the X-rays by Wilhelm Conrad Röntgen. He realized that X-rays travel through the skin and reveal the internal bone structure lying behind the tissue. His first image was produced in 1895 by chance. The photograph belonged to his wife's hand which is shown in Figure 1.1. Röntgen's authentic discovery captivated people's recognition worldwide, and he won the first Nobel Prize in physics in 1901 [1].

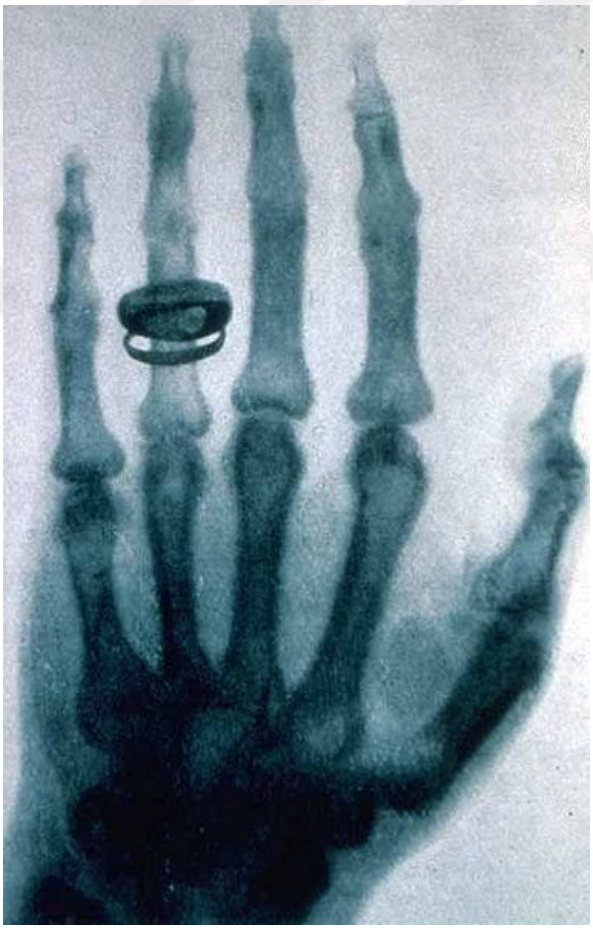

Figure 1.1. The first X-rays image taken by Röntgen, that shows Anna Bertha's left hand with a ring.

Until the invention of X-rays as a medical imaging modality, illness detection and diagnosis methods were limited with trial and error. The developments in med-

ical imaging modalities have provided both investigation through the human and the detection of abnormalities.

The fundamental intention of medical imaging is to produce images of the tissues' internal structures based on the principles of physics, mathematics, engineering, and biology. These images provide illness detection, identification of the mechanical conditions, and functions of the tissues. The goal of clinical imaging is to develop image quality and identify and cure the conditions in the early stages.

2. ULTRASOUND IMAGING

Ultrasonic spectrum is defined as the frequency above the 20 kHz up to 1 GHz. The ultrasonic waves can diffuse into materials and scatter from them. Further, the ultrasonic transducers are relatively low-priced and reliable sources for imaging. For detection, diagnosis, and prognosis, frequencies of the ultrasound waves in medicine range from 1 to 15 MHz. The proper one is chosen depending on the location of the target tissue, depth penetration, and spatial resolution. [2–4]

Ultrasonic frequencies have been analyzed to enhance the resolution of the image. High-frequency ultrasound imaging provides micrometer resolution. Besides the tissues' imaging details, the ultrasound imaging assesses to analyze the tumor evolution mechanism and the impacts of the medicine [5, 6] without additional preparations like staining.

2.1. Historical Development of the Acoustics

In nature, some animals emit acoustic waves and listen to their echoes to figure out the objects located around them. This feature is known as animal echolocation which is also known as bio-sonar. In 1794, Lazzaro Spallanzani, a biologist and physiologist, noticed the first time that bats could avoid the obstacles while flying in the dark [7].

After the discovery of the piezoelecricity by Curie brothers in 1880, small mechanical displacements can be converted into electricity and provides electrical signals. [8]. The piezoelectric effect is reversible, which means that materials can exhibit not only the direct piezoelectric effect but also the converse piezoelectric effect.

Langevin studied underwater transducers due to threatening the submarine in World War I [9]. Thus, he worked with high frequencies to detect objects underwater. Initially, the signals were too powerful that killed fishes in the experiment [10]. He then used a piezoelectric transducer with a quartz lens that is the first model of

piezoelectricity in an apparatus [11].

2.2. Ultrasound Applications

Researchers have been developed ultrasonic applications in various fields, from industrial usage to biological needs. Ultrasonic waves have been used to recognize the unseen cracks, irregularity in the crystals, leak spot, and the compounds of the involved materials in the industrial applications [12, 13].

Several therapeutic and diagnostic imaging methods had been developed such as Positron Emission Tomography (PET), Magnetic Resonance Imaging (MRI), and Computed Tomography (CT). Tomography demonstrates the sections of the tissues, and functional magnetic resonance imaging (fMRI) displays brain metabolic actions related to blood flow [14]. On the other hand, ultrasound imaging offers low-cost real-time imaging without applying ionizing radiation to the tissue [3].

2.3. Theory

A wave is a disturbance of the medium which transports energy and momentum [15]. Waves move through the medium, and they have different speeds in different media. The wavelength, λ, is the distance that waves moved in one cycle. Frequency, ν is the number of travel wavelength per unit time . Amplitude is the maximum height of the wave in one cycle, the velocity of the wave given by the relation between frequency and wavelength:

$$\upsilon = \nu\lambda \tag{2.1}$$

where υ is the velocity in the medium [15]. The magnitude of the sound velocity also expressed as:

$$\upsilon = \sqrt{\frac{1}{\kappa\rho}} \tag{2.2}$$

where κ is the compressibility, and ρ is the density of the surrounding [16]. The acoustics waves established as three-dimensional (3D) time-dependent differential equations as in Equation 2.3.

$$\psi(\mathbf{r},t) = \psi_0 e^{i(\omega.t - \mathbf{k}.\mathbf{r})} \tag{2.3}$$

In this expression, ψ_0 is a constant, $\mathbf{k}$ is the wave number, ω is the angular frequency, and $\mathbf{r}$ is the direction of the wave propagation expressed as:

$$\mathbf{r}^2 = \mathbf{x}^2 + \mathbf{y}^2 + \mathbf{z}^2 \tag{2.4}$$

where $\mathbf{x}$, $\mathbf{y}$, $\mathbf{z}$ are vectors. The wave equation is given as;

$$\nabla^2\psi(\mathbf{r},t) = \frac{1}{c^2}\frac{\partial^2}{\partial t^2}\psi(\mathbf{r},t) \tag{2.5}$$

where Laplacian operator is represented as following:

$$\nabla^2 = \frac{\partial^2}{\partial r^2} \tag{2.6}$$

$$\nabla^2\psi(\mathbf{r},t) = \left(\frac{\partial^2}{\partial x^2} + \frac{\partial^2}{\partial y^2} + \frac{\partial^2}{\partial z^2}\right)\psi(\mathbf{r},t) \tag{2.7}$$

For simplicity, consider the wave equation in one dimension, z-axis, and one can calculate as:

$$\frac{\partial^2}{\partial z^2}\psi(z,t) = \frac{1}{c^2}\frac{\partial^2}{\partial t^2}\psi(z,t) \tag{2.8}$$

$$\frac{\partial^2}{\partial z^2}\psi(z,t) = -\frac{{\omega_z}^2}{c^2}\psi(z,t) \tag{2.9}$$

Similarly, the same calculations can be repeated for each direction:

$$\frac{\partial^2}{\partial x^2}\psi(x,t) = -\frac{{\omega_x}^2}{c^2}\psi(z,t) \tag{2.10}$$

$$\frac{\partial^2}{\partial y^2}\psi(y,t) = -\frac{{\omega_y}^2}{c^2}\psi(y,t) \tag{2.11}$$

Acoustic impedance, Z, defined as the correlation between acoustic pressure, $p(\mathbf{r},t)$, and the particle's velocity, $\upsilon(\mathbf{r},t)$ [17], is given by:

$$Z = \frac{p(\mathbf{r},t)}{\upsilon(\mathbf{r},t)} \tag{2.12}$$

By rearranging Equations 2.2 and 2.12, the acoustic impedance formula becomes:

$$Z = \rho\upsilon \tag{2.13}$$

The acoustic impedance introduces the elastic properties of the medium that sound propagates. The units of the acoustic impedance are pascal second per cubic metre, $Pa.s.m^{-3}$ or the rayl per square metre, $Rayl.m^{-2}$. Rayl is stands for spesific acoustic impedance that is pascal second per meter, $Pa.s.m^{-1}$.

If acoustic pressure propagates through the medium, diversity in the mechanical characteristics begin to the ultrasound waves experiencing reflection, transmission, refraction, absorption, and scattering.

Assume that acoustic wave, ψ_i, is coming from left. When the wave is impinging the interface, it reflects, ψ_r, and transmitted, ψ_t, as shown in Figure 2.1. The incident wave, the reflected wave, and the transmitted wave can be formulated as follows:

$$\psi_i(\mathbf{r},t) = A_i e^{i\omega t - \mathbf{k}.\mathbf{r}} \tag{2.14}$$

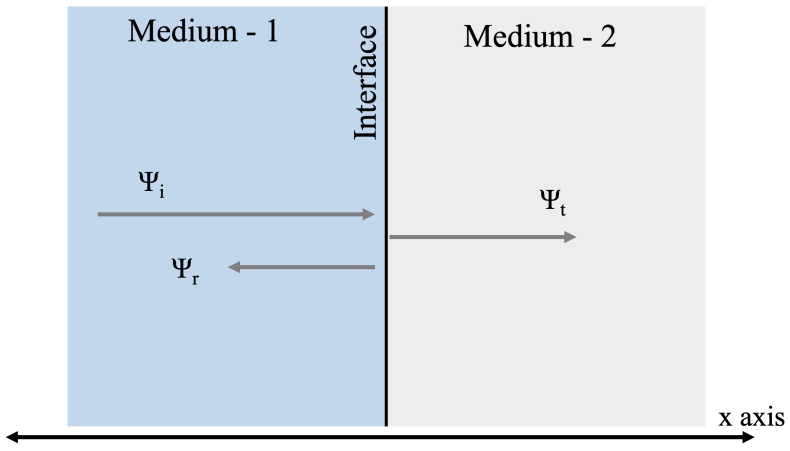

Figure 2.1. The acoustic wave propagation in the different media.

$$\psi_r(\mathbf{r},t) = A_r e^{i\omega t + \mathbf{k}.\mathbf{r}} \tag{2.15}$$

$$\psi_t(\mathbf{r},t) = A_t e^{i\omega t - \mathbf{k}.\mathbf{r}} \tag{2.16}$$

In these equations, A_i, A_t, and A_r are the acoustic pressure wave with an amplitude of incident, transmitted, and reflected wave, respectively. The ratio of the amplitudes gives the reflection coefficient,R, and the transmission coefficient, T.

$$R = \frac{A_r}{A_i} \tag{2.17}$$

$$T = \frac{A_t}{A_i} \tag{2.18}$$

Due to the continuity conditions, the correlation between the amplitude of the pressures and the velocity can be written as:

$$A_r + A_i = A_t \tag{2.19}$$

$$\upsilon_r + \upsilon_i = \upsilon_t \tag{2.20}$$

Dividing these equations delivers:

$$\frac{A_r + A_i}{\upsilon_r + \upsilon_i} = \frac{A_t}{\upsilon_t} \tag{2.21}$$

Using the acoustic impedance formula, one can introduce new impedance values:

$$\frac{A_i}{\upsilon_i} = \rho_1 \upsilon_1 \tag{2.22}$$

$$\frac{A_r}{\upsilon_r} = -\rho_1 \upsilon_1 \tag{2.23}$$

$$\frac{A_t}{\upsilon_t} = \rho_2 \upsilon_2 \tag{2.24}$$

where ρ_1 and ρ_2 are the densities, and υ_1, and υ_2 are the velocities with respect to medium-1 and medium-2. Since the reflected velocity, υ_r, travels in the opposite direction of the incident, minus sign comes up. Substituting these expressions into Equation 2.21 and reamending provides normal incidence pressure reflection coefficient as well as the transmission coefficient [17]:

$$R = \frac{\rho_2 \upsilon_2 - \rho_1 \upsilon_1}{\rho_2 \upsilon_2 + \rho_1 \upsilon_1} = \frac{Z_2 - Z_1}{Z_2 + Z_1} \tag{2.25}$$

$$T = \frac{2\rho_2 \upsilon_2}{\rho_2 \upsilon_2 + \rho_1 \upsilon_1} = \frac{2Z_2}{Z_2 + Z_1} \tag{2.26}$$

The interaction of sound waves with the material is also defined by absorption. The acoustic wave propagates through the body; ultrasound wave pressure loses its intensity with the distance covered, considering the vibrational energy is converted

into heat. This procedure is named as absorption. It likewise depends on the sample involved [2]. Besides absorption, attenuation can also be recognized while waves are scattering, reflecting, and heat-dissipating. The attenuation relies on the frequency magnitude of the ultrasonic wave. Thus, the high-frequency ultrasound waves amplitude diminishes immediately. It also depends on the type of tissue; it is higher for denser and harder tissues and is lower for soft tissues.

The scattering is a nonlinear concept that refers to the reflection of sound from surfaces in a medium. The acoustic scattering is essential for ultrasound imaging because changes in the target's mechanical characteristics cause waves to scatter. Acoustic scattering happens if a sound wave reaches structures within a target, where the size of the wavelength is smaller than the size of the structures. When the wavelength is greater than the scatterer's characteristic size, $a \approx 20\mu m$, $\lambda \gg a$, diffusive scatting detected and such Rayleigh scattering is very weak. If $\lambda \approx a$, $a \approx 0.1 - 1mm$ a frequency dependent diffractive scattering is noticed. When $\lambda > a$, it is the elementary reflection that can be examined in large samples, and it is not wavelength dependent.

2.4. Boundary Conditions at Interface

The medium carries sound from one medium to another. Due to the unique acoustic properties of a medium, incoming wave is not only reflected but also transmitted. Additionally, there is a relation between the angle of the incident wave, the refractive index of the medium, and the sound velocities in each media. Snell's law states that the ratio of the sines of the angles is equal to the ratio of refractive indexes and sound wave speeds in the media.

$$\frac{sin\theta_i}{sin\theta_t} = \frac{n_1}{n_2} = \frac{\upsilon_1}{\upsilon_2} \tag{2.27}$$

where n_1 and n_2 are the refractive indexes and υ_1 and υ_2 are the wave speed of the medium-1 and medium-2 respectively, shown in Figure 2.2.

Snell's law requires that the wave vectors should be continuous at the interface.

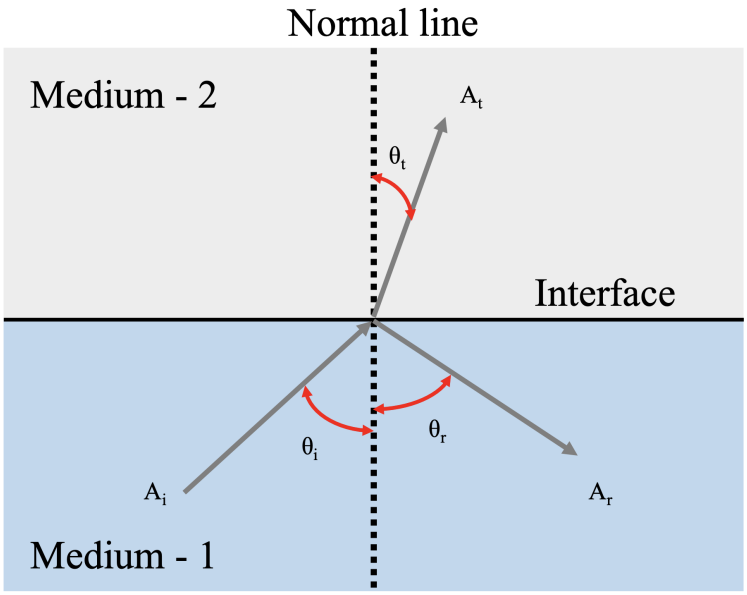

Figure 2.2. Schematic description of the Snell's law for the incident, reflected, and transmitted ultrasound waves.

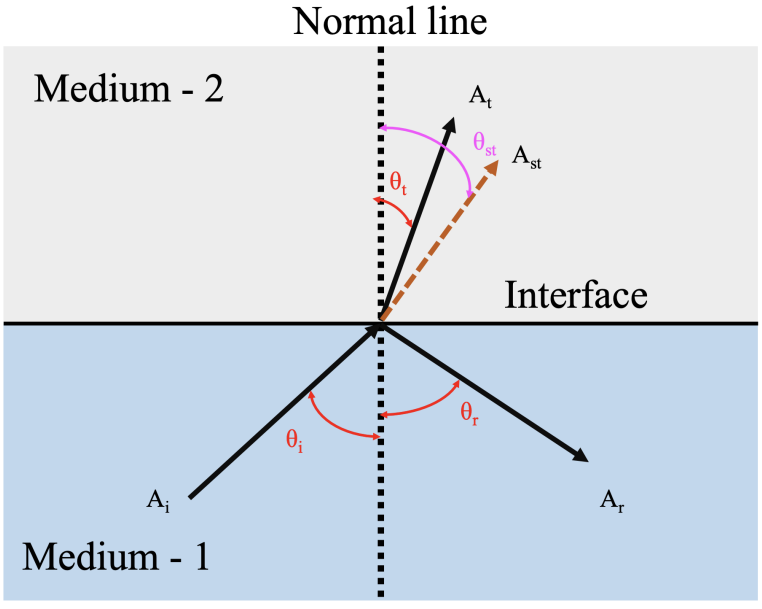

Figure 2.3. Schematic description of propagating the shear waves for liquid-solid interface.

For the investigation of the sound propagation, estimations of the reflection and transmission coefficients get more uncertain due to the pressure and shear waves of the incident, reflected and transmitted waves. In the liquid-solid border, pressure and potential must be equal to satisfy the boundary conditions. However, for liquid medium, shear waves are ignored due to their weak bounding characteristic. Consequently, the incident and reflected waves individually occur in a liquid layer, as illustrated in Figure 2.3 [2, 18, 19].

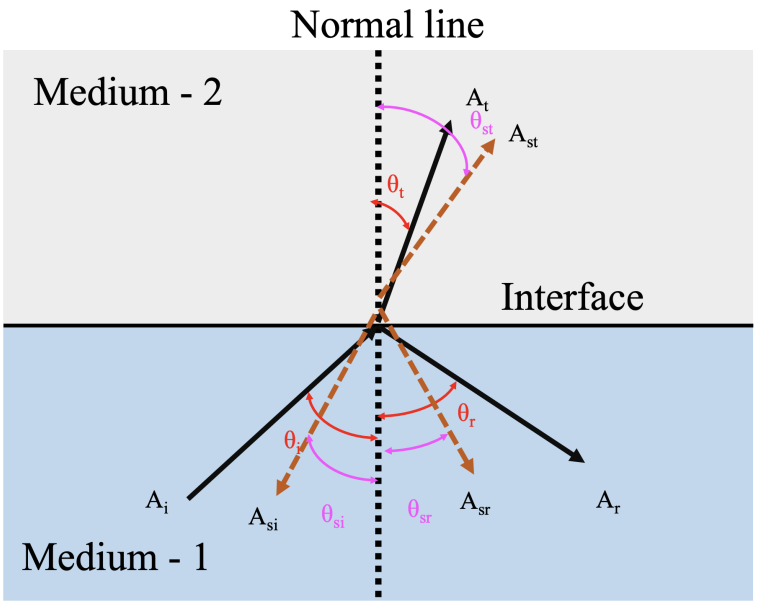

Figure 2.4. Schematic description of propagating the shear waves for solid-solid interface.

Shear wave has been considered for solid media that travels both media, as shown in Figure 2.4. The incoming wave in the x-z plane can written as following [18].

$$\psi_i(x, z; t) = A_i e^{i[\omega t + k_{x1}.x - k_{z1}.z]} \tag{2.28}$$

Since the angles are known, the Equation 2.28 can be rewritten in terms of the sine and cosine functions:

$$\psi_i(x, z; t, t) = A_i e^{i[\omega t + k_{x1} sin\theta_i x - k_{z1} cos\theta_i z]} \tag{2.29}$$

$$\psi_i(x,z;t,t) = A_i e^{i[\omega t + k_{L1} sin\theta_i x - k_{L1} cos\theta_i z]} \tag{2.30}$$

$$\psi_s i(x,z;t,t) = A_s i e^{i[\omega t + k_{S1} sin\theta_s i x - k_{S1} cos\theta_s i z]} \tag{2.31}$$

where k_{L1}, and k_{S1} are the wave numbers for liquid and solid media, respectively. One can write the wave equations for the reflected waves and reflected shear waves similarly.

$$\psi_r(x,z;t,t) = A_i e^{i[\omega t + k_{L1} sin\theta_r x - k_{L1} cos\theta_r z]} \tag{2.32}$$

$$\psi_s r(x,z;t,t) = A_s r e^{i[\omega t + k_{S1} sin\theta_s r x - k_{S1} cos\theta_s r z]} \tag{2.33}$$

Also, one can calculate the wave equations for the transmitted waves and transmitted shear waves similarly.

$$\psi_t(x,z;t,t) = A_t e^{i[\omega t + k_{L1} sin\theta_t x - k_{L1} cos\theta_t z]} \tag{2.34}$$

$$\psi_s t(x,z;t,t) = A_s t e^{i[\omega t + k_{S1} sin\theta_s t x - k_{S1} cos\theta_s t z]} \tag{2.35}$$

2.5. Scanning Acoustic Microscopy (SAM)

SAM is a type of ultrasonic imaging technique that measures acoustic impedance (AI) and the speed of sound (SOS) at micrometer resolution. AI and SOS modes are tissue-specific and give the biomechanical properties of samples. The system in our lab is shown in Figure 2.5.

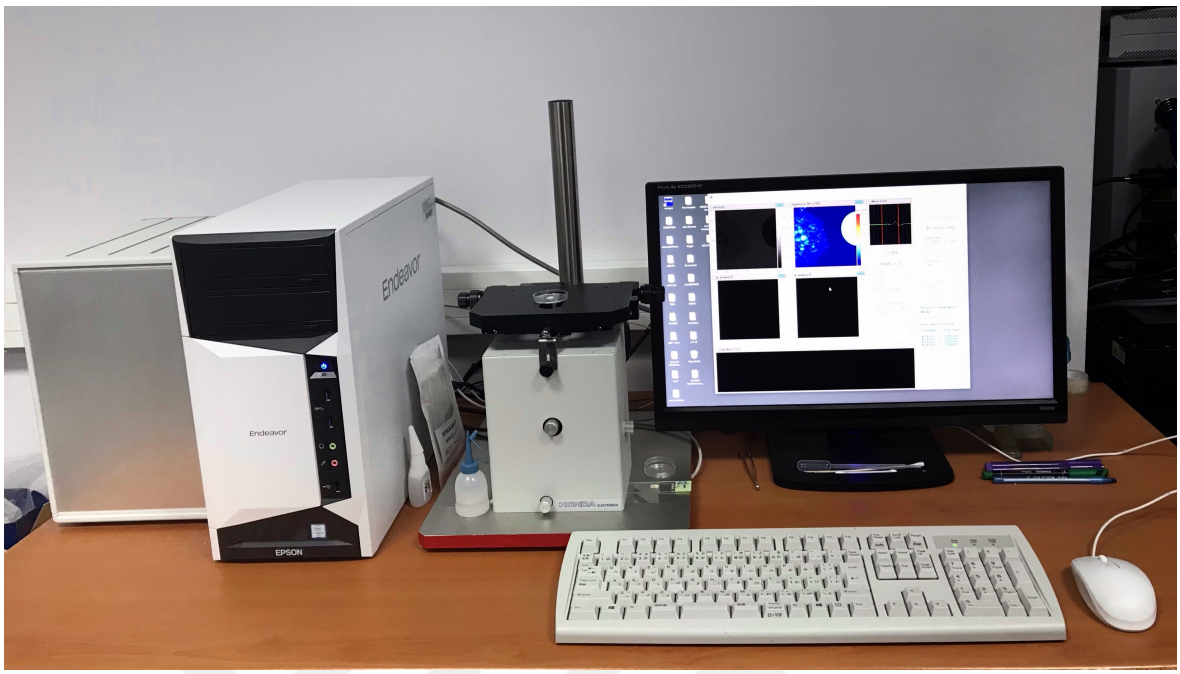

Figure 2.5. The photograph of SAM (Ultrasonic Microscope AMS – 50SI) in our lab.

SAM sends high-frequency ultrasonic waves to biological specimens and determines their acoustic impedance map in the SOS or AI mode.

An SAM system consists of a transducer, an acoustic probe, an oscilloscope, and a computer with software shown in Figure 2.6. Ultrasound waves are produced by a transducer, and then they are focused on a polystyrene slide. The acoustic waves are transmitted through the coupling medium to the sample. The acoustic waves are reflected from both the polystyrene slide and the specimen. The back-reflected sound waves are also collected by the same transducer while scanning over the target region. Finally, the acoustic impedance image of the sample is generated in the order of minutes.

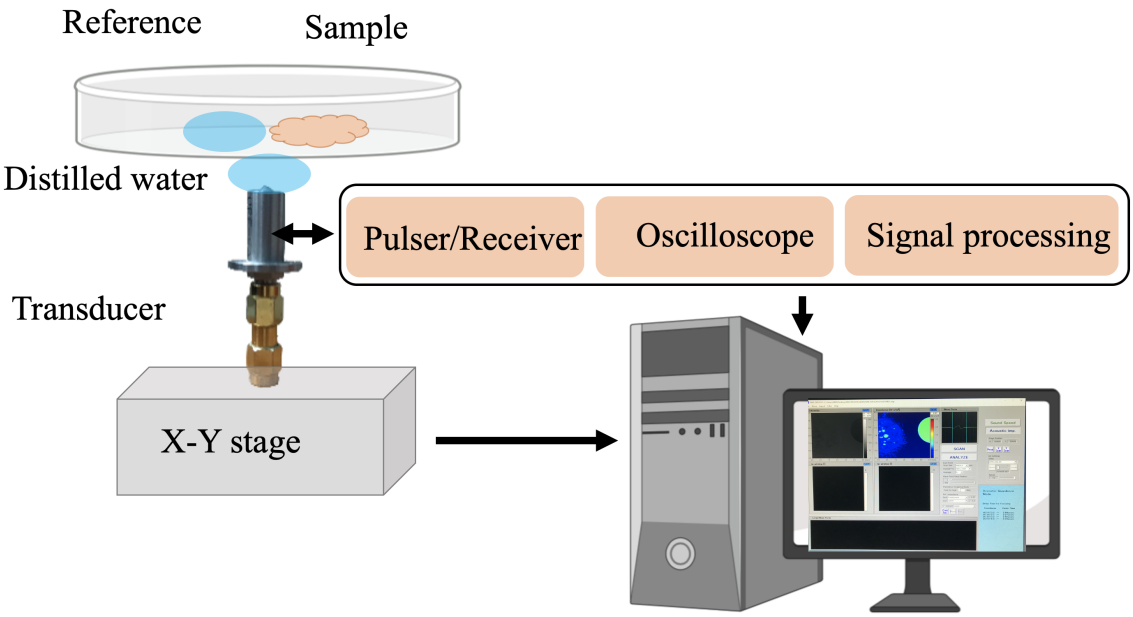

Figure 2.6. Demonstration of the system setup. The system consists of a high-frequency transducer, an acoustic probe, an oscilloscope, and a computer with software.

The system facilitates an 80 MHz and a 320 MHz transducer. Depending on the sample of interest, one of these transducers is used to perform the imaging session.

The 80 MHz transducer is spherically focused that is built by piezoelectric polymer, polyvinylidene fluoride trifluoroethylene (PVDF-TrFE) thin film [20,21]. 80 MHz transducer has a spot size of 17 μm and a focal length of 1.5 mm. The bandwidth of the transducer is ranging from 50 to 105 MHz, and the signals are averaged by eight times used for tissue imaging studies.

The high frequency, 320 MHz transducer which consists of a flat ZnO as piezoelectric material attached with a uniform sapphire lens of half curvature of 60°. Its aperture diameter and focal length from the bottom of the lens are 1.2 and 0.29 mm, respectively. The bandwidth frequency of the transducer is between 200 - 400 MHz. This transducer is usually used for imaging of cell cultures.

The ultrasonic waves propagate through several layers; coupling medium, polystyrene substrate, and the sample. It returns to the substrate-target interface. The acoustic images show the boundary line between the sample and the substrate's back surface.

In the acoustic impedance measurement mode, the reference signal's measurement is formulated in Equation 2.36 [20]:

$$S_{Reference} = \frac{Z_{Reference} - Z_{Substrate}}{Z_{Reference} + Z_{Substrate}} S_0 \tag{2.36}$$

where S_0 and $S_{Reference}$ represent signals generated by the transducer, reflected signal from the distilled water, respectively and demonstrated in Figure 2.7.

$$S_{Sample} = \frac{Z_{Sample} - Z_{Substrate}}{Z_{Sample} + Z_{Substrate}} S_0 \tag{2.37}$$

where S_{Sample} stands for the reflected sample signal. Then, the acoustic impedance of

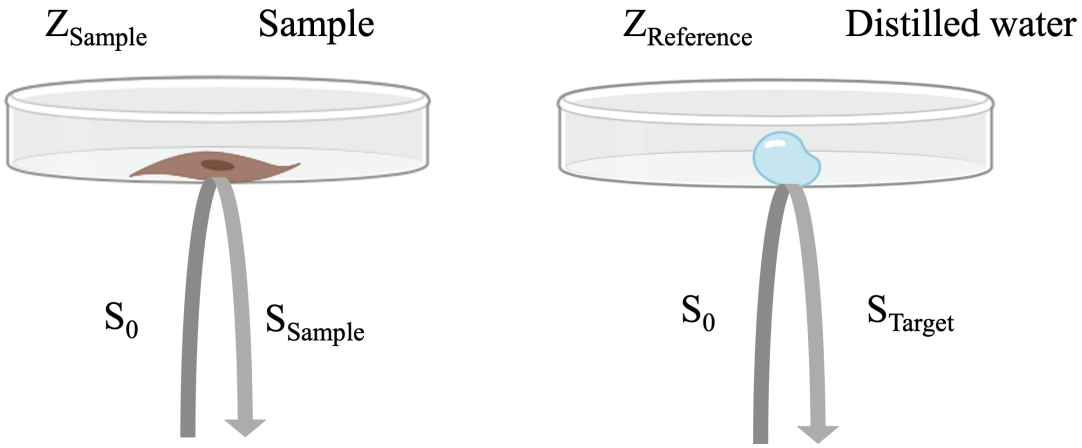

Figure 2.7. Principle of acoustic impedance mode of the SAM. A transducer works in pulse/echo mode. The acoustic wave reflects from the surfaces of reference and the data are collected by the transducer.

the sample is calculated from Equations 2.36 and 2.37 as follows:

$$Z_{Sample} = \frac{1 - \frac{S_{Sample}}{S_0}}{1 + \frac{S_{Sample}}{S_0}} Z_{Substrate} \tag{2.38}$$

$$Z_{Sample} = \frac{1 - \frac{S_{Sample}(Z_{Substrate} - Z_{Reference})}{S_{Reference}(Z_{Substrate} - Z_{Reference})}}{1 + \frac{S_{Sample}(Z_{Substrate} - Z_{Reference})}{S_{Reference}(Z_{Substrate} - Z_{Reference})}} Z_{Substrate} \tag{2.39}$$

At the beginning of the imaging session, the setup is calibrated with a signal read from the substrate. The focused transducer generates the pulse and then collects the echo signal from a reflecting body. It insonates and investigates the restricted zone below the polystyrene substrate holding the focal point on the substrate's back surface [2].

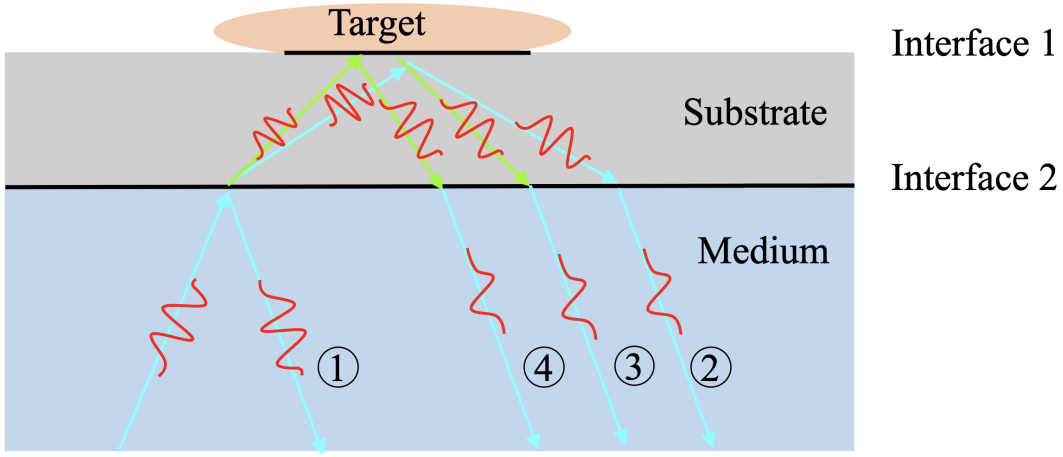

Figure 2.8. The path of waves from the boundary lines emerged from water-substrate and substrate-target.

The sample is displayed with the reference material in the same region. The ultrasound pulses are obtained from the surface of the target after moving through the substrate, having a finite attenuation, during the acoustic impedance measurement. As an outcome, the reflected waves from the target and the reference material are analyzed. The comparison of the target's signals and the reference's signals reveals on the oscilloscope, which is converted to an acoustic impedance map by using Fourier Transformation. Thus, signals are obtained in the frequency domain to interpret the acoustic impedance.

Furthermore, in the sound speed measurement mode, the target is fixed on the substrate and the substrate is located upside-down on the microscope over the ultrasound probe as shown in Figure 2.9 . Ultrasonic wave transmitted from the probe is used upward towards the glass substrate. Ultrasonic waves pass through the thin-flat target directly, contacting the ultrasonic transducer via the coupling fluid. The wave reflects at the plane interface between the target-substrate layer and reflects from the target's anterior surface. In this mode, one can identify the acoustic intensity, sound

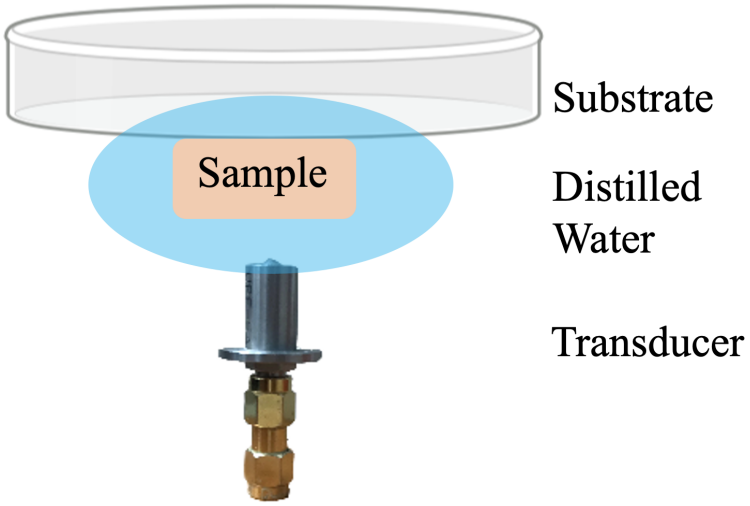

Figure 2.9. Demonstration of sample fixation in SOS mode.

speed, attenuation, and thickness variables of the sample.

3. RAMAN SPECTROSCOPY

Spectroscopy is a technique that scrutinizes the fundamental interactions between materials and electromagnetic radiations. It identifies individual samples at the molecular level and gives information about the molecule's chemical characteristics.

Sir C.V. Raman discovered Raman spectroscopy in 1928 [22], and he won the Nobel Prize in Physics for his study and the discovery of the new phenomenon in 1930 [23].

Raman spectroscopy has different applications fields from art and archaeological identifications [24, 25] to biomedical studies [24–26].

Raman Spectroscopy is a procedure to discover vibrational modes of the matter that is illuminated with a light source. The Raman effect is identified when a molecule interacts with a light source, and electrons are excited. While photon is interacted with a material, an electron is pumped to a virtual energy level in short notice, and a molecule is in the different vibrational or rotational state. Hence, the Raman effect is investigated as a scattering of the light by elements. If the scattering procedure is observed as an elastically scattering, energy is preserved, as well as the frequency is not altered that is named Rayleigh scattering.

The process, despite, can be inelastic scattering, which is generally weak. In this situation, Stokes or anti-Stokes scattering can be seen. If the system loses energy, the Stokes scattering is detected. If the energy of the scattered photon increases comparing to incoming photons, anti-Stokes scattered is examined. Since the molecule's energy state is changed in the inelastic collision, the energy of the scattered photons is also modified. If the total energy is higher than the initial energy, the Stokes shift appears. Otherwise, the anti-Stokes shift is observed. The Jablonski diagram as a function of energy is exhibited in Figure 3.1.

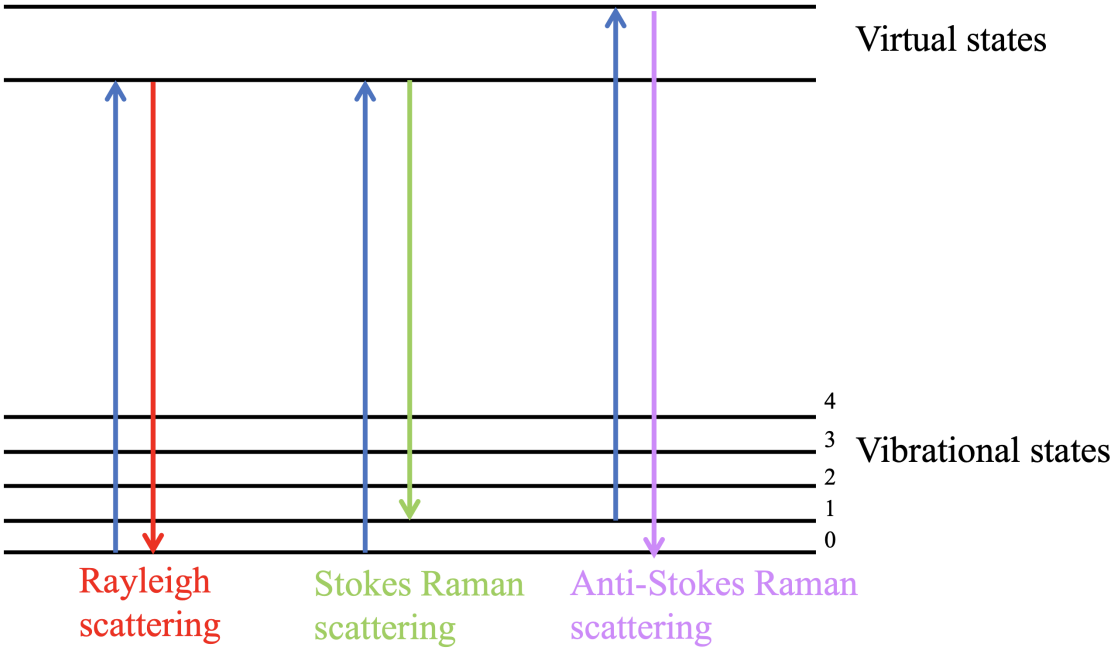

Figure 3.1. Raman energy levels.

The electric field at a given time is represented by

$$E = E_0 cos(2\pi\nu t) \tag{3.1}$$

where E_0 is the amplitude of the electric field and ν is the frequency of the wave. Recall that the formula of the frequency, which has unit Hertz (Hz).

$$\nu = \frac{c}{\lambda} \tag{3.2}$$

where c is the velocity of light, and λ is the wavelength. The inverse of the frequency is called wavenumber, $\bar{\nu}$, that is associated with the vibrational spectra of the molecules. The unit of wavenumber is cm^{-1}, and the wavenumber is calculated as;

$$\bar{\nu} = \frac{1}{\lambda} \tag{3.3}$$

If a particle interacts with an electromagnetic field, energy is transferred from photon

to the particle.

$$\Delta E = h\nu = h\frac{c}{\lambda} = hc\bar{\nu} \tag{3.4}$$

ΔE describes the energy separation in two quantized states, and h is the Plank's constant. ΔE is also defined as:

$$\Delta E = E_2 - E_1 \tag{3.5}$$

where E_1 and E_2 are first and second energy states, respectively.

In Raman spectroscopy, the specimen is irradiated by a light source in the UV-visible range. The scattered light is commonly perceived in the direction perpendicular to the incident beam shown in Figure 3.2 [27]. As a result, two different scattering types

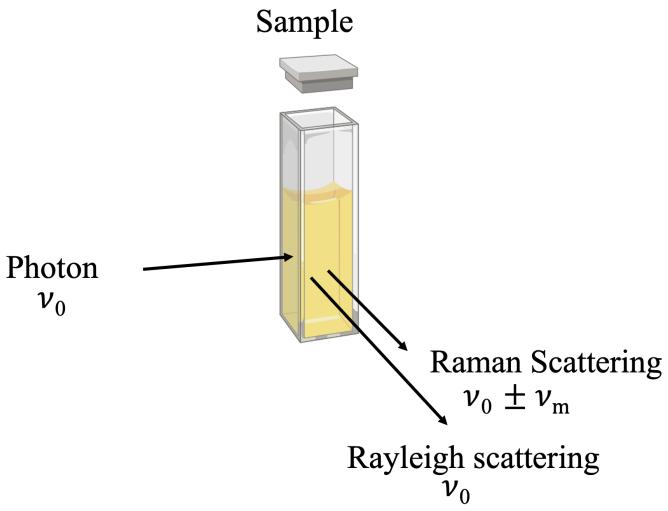

Figure 3.2. Raman spectroscopy process

are seen; Rayleigh scattering has a frequency of ν_0 and Raman scattering. The Stokes and anti-Stokes lines are observed in the Raman scattering that their frequencies altered as $\nu_0 - \nu_m$ and $\nu_0 + \nu_m$, respectively.

The electric field fluctuates with time, t.

$$E = E_0 cos(2\pi\nu_0 t) \tag{3.6}$$

where E_0 is the vibrational amplitude, and ν_0 is the frequency of the beam originating from the laser. If the laser irradiates the molecule, an electric dipole moment P is produced:

$$P = \alpha E = \alpha E_0 cos(2\pi\nu_0 t) \tag{3.7}$$

α is named polarizability. If the diatomic molecule moves with vibrating frequency ν_m, the nuclear displacement q is observed:

$$q = q_0 cos(2\pi\nu_m t) \tag{3.8}$$

where q_0 is vibrational amplitude. Also, polarizability is a function of nuclear displacement. For small vibrational amplitude, polarizability can be written as follows:

$$\alpha = \alpha_0 + \left(\frac{\partial\alpha}{\partial q}\right) + q_0 + ... \tag{3.9}$$

α_0 is the polarizability at the balance, and $\left(\frac{\partial\alpha}{\partial q}\right)$ is the rate of change concerning the variation in q, evaluated at the equilibrium position. Consequently, polarizability can be expanded as:

$$P = \alpha_0 E_0 cos(2\pi\nu_0 t) + \left(\frac{\partial\alpha}{\partial q}\right) q_0 E_0 cos(2\pi\nu_0 t) cos(2\pi\nu_m t) \tag{3.10}$$

$$P = \alpha_0 E_0 cos(2\pi\nu_0 t) + \frac{1}{2}\left(\frac{\partial\alpha}{\partial q}\right) q_0 E_0 [cos2\pi(\nu_0 + \nu_m)t + cos2\pi(\nu_0 - \nu_m)t] \tag{3.11}$$

The first term defines an oscillating dipole that radiates light of frequency ν_0, Rayleigh scattering, classically. The next term is associated with Raman scattering. If the rate of

change of polarizability, $\left(\frac{\partial \alpha}{\partial q}\right)$, is grater than to zero, the vibration is Raman-active [27].

The polarizability nature of the particle should be considered to explain the Raman activity. When the sample is placed under the intense laser beam, charged particles attracted to each other due to the electric field. The separation of the positive and negative charges produces an induced dipole moment, P demonstrated in Equation 3.7. Since the electric field and polarizability are vector and have three components in each direction, the Equation 3.7 can be rewritten in matrix form:

$$\begin{bmatrix} P_x \\ P_y \\ P_z \end{bmatrix} = \begin{bmatrix} \alpha_{xx} & \alpha_{xy} & \alpha_{xz} \\ \alpha_{yx} & \alpha_{yy} & \alpha_{yz} \\ a\alpha_{zx} & \alpha_{zy} & \alpha_{zz} \end{bmatrix} \begin{bmatrix} E_x \\ E_y \\ E_z \end{bmatrix} \tag{3.12}$$

In Equation 3.12, the first matrix on the hand side is known as polarizability tensor. If $\alpha_{xy} = \alpha_{yz}$, $\alpha_{xz} = \alpha_{zx}$, and $\alpha_{yz} = \alpha_{zy}$, the matrix is symmetric and Raman scattering is seen. If these components are varied during the vibration, it is Raman-active.

Furthermore, the Raman spectrum of the water is weak. Thus, the Raman spectra of the aqueous samples can be collected without significant obstruction from water. Consequently, Raman spectroscopy is a practical method for the examination of biological specimens.

Our RS laboratory setup consists mainly of three parts: optical microscope (Nikon Ti), Raman spectrometer (Ocean QE Pro), and the laser source (Laser Glow, 785 nm, 500 mW). The laser source is pointed into the sample plane to excite the electrons in the sample. The back-scattered photons are obtained using the same optics. The inelastically scattered photons are elected using a dichroic mirror (Thorlabs DMSP 805). They are focused on the spectrometer after the further filtration of the Rayleigh photons by two sequential long pass filters (Thorlabs FELH805).

4. NANOPARTICLES

4.1. Semiconductors

The electrons are subatomic particles generally in the lowest energy band due to the Pauli Exclusion Principle. Conduction band and valence band with the electrons determine the material's electronic properties. The former is empty of charges that are excited states for the electrons, and the valence band is full of negative charges.

Conductors are not true metals, because ΔE_{gap} is very small and and carries can easily excited. On the contrary, the insulators' energy difference between the conduction band and valence band is enormous so the conduction band is empty. Thus, insulators cannot contribute to producing current. The semiconductors are solid crystals that have intermediate electric conductivity between metals and insulators.

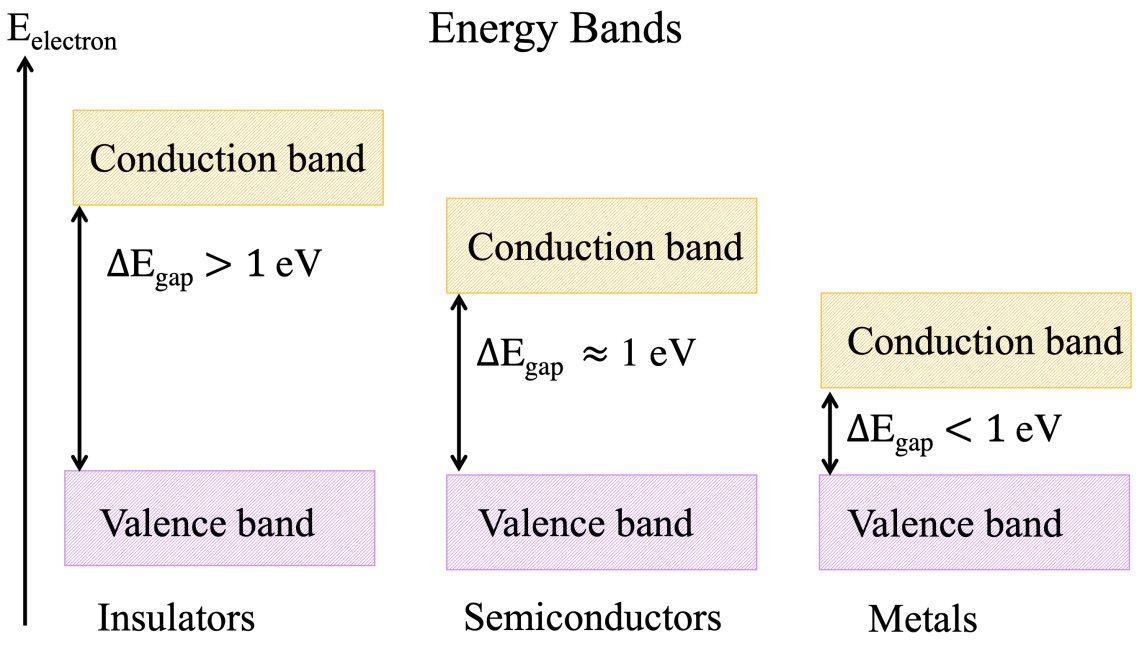

Figure 4.1. Representation of energy bands of insulators, semiconductors, and metals.

When a photon's energy is equal or higher than the bandgap, it can promote an electron from valence band to conduction band in a semiconductor. Therefore, an electron can absorb a photon and jump to the conduction band and abandons a hole, as illustrated in Figure 4.2. The hole acts as a positive charge and interacts with the excited electron, then the electron goes back to the valence band and emits a photon.

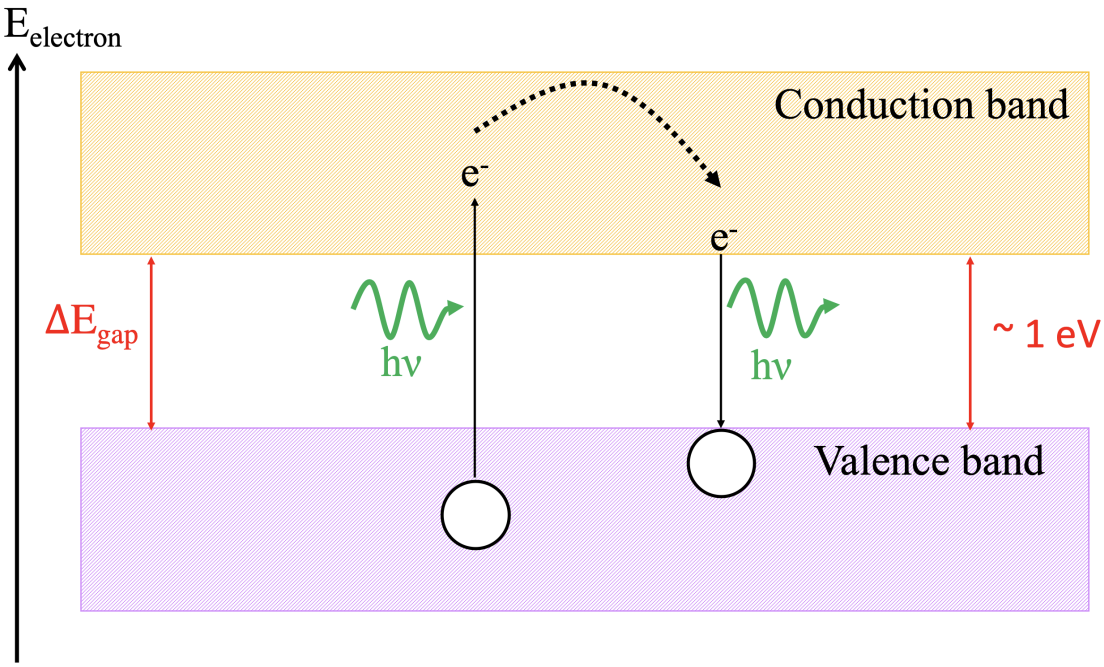

Figure 4.2. Representation of absorption and emission of photons processes for the semiconductor materials.

4.2. Quantum Wells

The quantum wells are one of the categories of the semiconductors that their particles are localized in a two-dimensional (2D) region by the quantum confinement effect, illustrated in Figure 4.3. The quantum confinement effect occurs when the size of the infinite well as compared to the wavelength of an electron. Quantum wells are described by a local minimum potential that has infinite potential and has all particles in ideally. Potential inside the well is taken to zero to solve the Schrödinger equation effortlessly:

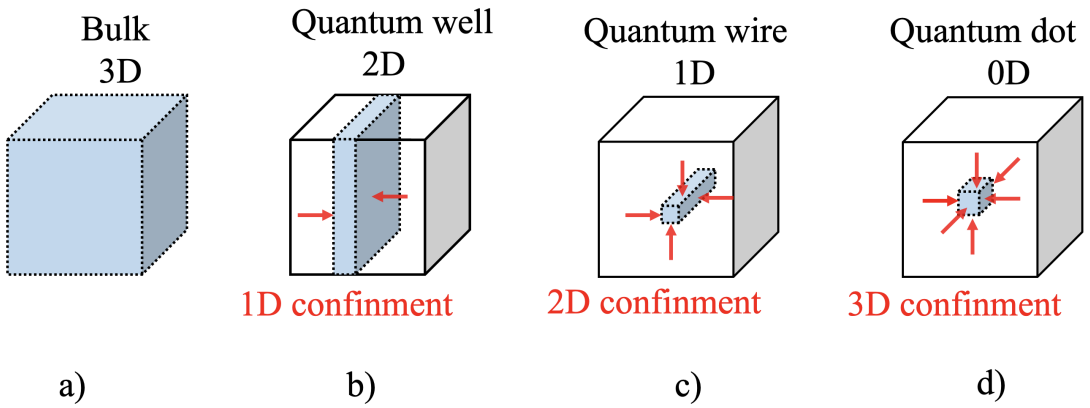

Figure 4.3. Demonstration of a) bulk semiconductors and quantum confinement effect for b) quantum wells, c) quantum wires, and d) quantum dots.

$$-\frac{\hbar^2}{2m}\nabla^2\psi(x,y,z)+V(x,y,z)\psi(x,y,z)=E(x,y,z)\psi(x,y,z) \tag{4.1}$$

Since potential is zero by convention, the one-dimensional (1D) Schrödinger equation becomes:

$$-\frac{\hbar^2}{2m}\frac{\partial^2}{\partial z^2}\psi(z)=E\psi(z) \tag{4.2}$$

Then, solution of the wave is found as a free particle:

$$\psi(\mathbf{r})=Ae^{i\mathbf{k}.z}+Be^{-i\mathbf{k}.z} \tag{4.3}$$

where magnitude of $\mathbf{k}$ is

$$|\mathbf{k}|=\frac{\sqrt{2mE}}{\hbar} \tag{4.4}$$

All particle should be in he well. Therefore, by the continuity condition

$$\psi(0)=\psi(d_z)=0 \tag{4.5}$$

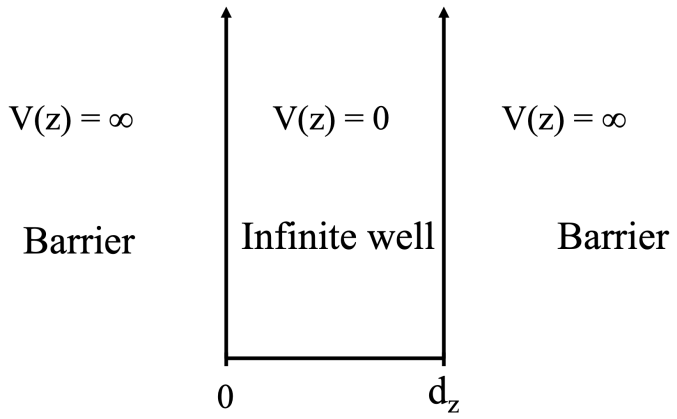

Figure 4.4. The infinite well

$$\psi(0) = A + B = 0 \tag{4.6}$$

$$A = -B \tag{4.7}$$

$$\psi(d_z) = Asin(k_z d_z) = 0 \tag{4.8}$$

$$k_z d_z = n\pi \tag{4.9}$$

$$k_z = \frac{n\pi}{d_z} \tag{4.10}$$

where n is the integer that stands for energy levels. From Equations 4.4 and 4.10 the total energy can be calculated:

$$E = \frac{\hbar^2 k_z^2}{2m} \tag{4.11}$$

The wave equation becomes:

$$\psi_n(z) = A_n sin(\frac{n\pi}{d}z) \tag{4.12}$$

By normalization A_n is calculated:

$$\int_{-\infty}^{+\infty} |\psi_n(z)|^2 = \int_{-\infty}^{+\infty} (A_n sin(\frac{n\pi}{d}|\mathbf{r}|))^2 = 1 \tag{4.13}$$

$$|A_n| = A = \sqrt{\frac{2}{d_z}} \tag{4.14}$$

Finally, wave equation is evaluated from Equation 4.3 to obtain:

$$\psi_n(z) = \sqrt{\frac{2}{d}} sin(\frac{n\pi}{d_z}z) \tag{4.15}$$

The energy can be stated as:

$$E = \frac{\hbar^2 n^2 \pi^2}{2md_z^2} \tag{4.16}$$

When the 1D potential is built from adjusted thin layers of different semiconductors, the particles can shift in the plane of the layers. [28]. Then, the Schrödinger equation becomes;

$$-\frac{\hbar^2}{2m}(\frac{\partial^2}{\partial x^2}\frac{\partial^2}{\partial y^2}\frac{\partial^2}{\partial z^2})\psi + V\psi = E\psi \tag{4.17}$$

where the potential and the total energy are respectively given by:

$$V = V(z) \tag{4.18}$$

$$E = E(x) + E(y) + E(z) \tag{4.19}$$

By separation of variables, the wave function can be also written as:

$$\psi = \psi(x)\psi(y)\psi(z) \tag{4.20}$$

Solving Equation 4.17, the following equations are obtained for each axis:

$$-\frac{\hbar^2}{2m}\frac{\partial^2}{\partial x^2}\psi(x) = E(x)\psi(x) \tag{4.21}$$

$$-\frac{\hbar^2}{2m}\frac{\partial^2}{\partial y^2}\psi(y) = E(y)\psi(y) \tag{4.22}$$

$$-\frac{\hbar^2}{2m}\frac{\partial^2}{\partial z^2}\psi(z) + V(z)\psi(z) = E(z)\psi(z) \tag{4.23}$$

For solving the Equation 4.21, the simple traveling wave equation is replaced as $\psi(x) = e^{ik_x x}$. Energy for the x-axis is found as:

$$E(x) = \frac{\hbar^2 {k_x}^2}{2m} \tag{4.24}$$

Likewise, energy for the y-axis is:

$$E(y) = \frac{\hbar^2 {k_y}^2}{2m} \tag{4.25}$$

Therefore, in-plane motion of the particle in a 1D confining potential summed as [28]

$$\psi_{x,y} = Ae^{[ik_x x + k_y y]} \tag{4.26}$$

$$E(x,y) = \frac{\hbar^2 {k_{x,y}}^2}{2m} \tag{4.27}$$

where

$$k_{x,y}{}^2 = k_x^2 + k_y^2 \tag{4.28}$$

Quantum wells have different roles in the field of lasers. They are used in quantum well lasers as laser diode. [29] In such lasers, the active region is so thin that quantum properties are tracked. Quantum wells are also used as semiconductor saturable absorbers in mode-lock semiconductor diode lasers. [30] Apart from the lasers, the solar cells with the quantum wells have great efficiency. [31]

4.3. Quantum Wires

A quantum wire is a semiconducting wire with a radius in the nanometer size that the quantum confinement effect is observed:

$$-\frac{\hbar^2}{2m}\nabla^2\psi(x,y,z) + V(x,y,z)\psi(x,y,z) = E(x,y,z)\psi(x,y,z) \tag{4.29}$$

In the quantum wire case, the confined potential energy and the wave function are written similar to the quantum well calculations where x and y axes are confined in Equation 4.29.

$$V(x,y,z) = V(x) + V(y) + V(z) \tag{4.30}$$

$$\psi(x,y,z) = \psi(x)\psi(y)\psi(z) \tag{4.31}$$

From the Schrödinger equation, decoupled equations were obtained:

$$-\frac{\hbar^2}{2m}\psi(y)\psi(z)\frac{\partial^2\psi(x)}{\partial x^2} + \psi(y)\psi(z)V(x)\psi(x) = E(x)\psi(x)\psi(y)\psi(z) \tag{4.32}$$

$$-\frac{\hbar^2}{2m}\psi(x)\left(\frac{\partial^2\psi(y)}{\partial y^2}\psi(z)+\psi(y)\frac{\partial^2\psi(z)}{\partial z^2}\right)+(V(y)+V(z))\psi(x)\psi(y)\psi(z) \\ =(E(y)+E(z))\psi(x)\psi(y)\psi(z) \tag{4.33}$$

Since, the potential equation in the x-axis is zero, equations become;

$$-\frac{\hbar^2}{2m}\frac{\partial^2\psi(x)}{\partial x^2}=E(x)\psi(x) \tag{4.34}$$

$$-\frac{\hbar^2}{2m}\left(\frac{\partial^2\psi(y)\psi(z)}{\partial y^2}+\frac{\partial^2\psi(y)\psi(z)}{\partial z^2}\right)+\psi(y)\psi(z)(V(y)+V(z))= \\ (E(y)+E(z))\psi(y)\psi(z) \tag{4.35}$$

For Equation 4.34, again plane-wave equation is placed, and energy is calculated:

$$E(x)=\frac{\hbar^2k_x^2}{2m} \tag{4.36}$$

Equation 4.35 demonstrates the quantum wire characteristics with 2D confined potential energy. [28] From Equation 4.35, one can obtain the following equations.

$$-\frac{\hbar^2}{2m}\frac{\partial^2\psi(y)}{\partial y^2}=E(y)\psi(y) \tag{4.37}$$

$$-\frac{\hbar^2}{2m}\frac{\partial^2\psi(z)}{\partial z^2}=E(z)\psi(z) \tag{4.38}$$

Recall that the potential is infinite, and the waves do not exist by the continuity condition outside of the wire. Therefore, the last equations are similar to equation 4.12. Therefore, the energy of the system for each direction is the following.

$$E(y)=\frac{\hbar^2n_y^2\pi^2}{2md_y^2} \tag{4.39}$$

$$E(z) = \frac{\hbar^2 n_z^2 \pi^2}{2md_z^2} \tag{4.40}$$

where n_y and n_z are the principal quantum numbers as distinct from quantum wells.

4.4. Quantum Dots

The quantum dots are also a type of semiconductor in the nanometer scale with 3D confinement potential. Their optical properties depend on both their sizes and shapes.

The potential is zero inside of the quantum dots, then the Schrödinger equation is written as:

$$-\frac{\hbar^2}{2m}\nabla^2\psi(x,y,z) = E(x,y,z,)\psi(x,y,z) \tag{4.41}$$

Once again, the equations of motion and energies are acquired for all directions.

$$-\frac{\hbar^2}{2m}\frac{\partial^2\psi(x)}{\partial x^2} = E(x)\psi(x) \tag{4.42}$$

$$-\frac{\hbar^2}{2m}\frac{\partial^2\psi(y)}{\partial y^2} = E(y)\psi(y) \tag{4.43}$$

$$-\frac{\hbar^2}{2m}\frac{\partial^2\psi(z)}{\partial z^2} = E(z)\psi(z) \tag{4.44}$$

$$E(x) = \frac{\hbar^2 n_x^2 \pi^2}{2md_x^2} \tag{4.45}$$

$$E(y) = \frac{\hbar^2 n_y^2 \pi^2}{2md_y^2} \tag{4.46}$$

$$E(z) = \frac{\hbar^2 n_z^2 \pi^2}{2md_z^2} \tag{4.47}$$

The total energy is the sum of the energies in all directions.

$$E(x,y,z) = \frac{\hbar^2 \pi^2}{2m}\left(\frac{n_x^2}{d_x^2} + \frac{n_y^2}{d_y^2} + \frac{n_z^2}{d_z^2}\right) \tag{4.48}$$

Once more, $n_x, n_y,$, and n_z are the principal quantum numbers for states.

Quantum dots are used in the imaging field as contrast agents or marker [32–34] and as drug delivery agents [35–37] due to their light stability, low toxicity, and the strong fluorescence intensity [38, 39]. Practicing non-toxic quantum dots as contrast agents in biomedical imaging applications such as magnetic resonance imaging [40], optical coherence tomography [41], positron emission tomography (PET), single-photon emission computed tomography, optical imaging, and photoacoustic imaging [42–44] demonstrate their capability as a powerful diagnostic agent.

Furthermore, the energy band structure of QDs transformed into quantized energy levels, and the sharp peaks in the absorption spectrum are observed [45–48]. Thus, one can tune the electronic states of semiconductors on the nanometer scale.

In various respects, QDs can probably combine the best properties of small molecule chromophores and bulk semiconductors [49]. As fluorophores, QDs are extremely bright, as well as almost each absorbed photon returns in an emitted fluorescence photon [50, 51]. In terms of photostability, organic dyes photobleach in seconds or minutes. Contrary to dyes, QDs illuminate up to hours [52, 53]. Moreover, organic dyes' absorption spectra are narrow, but QDs absorb photons that have higher energy than their energy gap. QDs also have short Stokes shifts; they can be excited at energies beyond their bandgap, making them much more adaptable for some applications.

5. SCANNING ACOUSTIC MICROSCOPY OF QUANTUM DOTS AGGREGATES

5.1. Materials and Methods

Orange and green emitting core-shell cadmium telluride/cadmium sulphide (CdTe/CdS), lead sulfide (PbS), and graphene nanocolloids (GQD) were obtained from Quantag Nanotechnologies (Istanbul, Turkey) in distilled water and used without further purification.The size of graphene and CdTe/CdS (green) QDs $\approx$ 2 nm, the size of PbS QDs $\approx$ 3 nm, and the size of CdTe/CdS (orange) QDs $\approx$ 5 nm with quantum efficiencies higher than 50 %. Approximately 10 μl of colloidal suspensions of QDs were dripped onto Petri dishes with a micro-pipette for SAM and fluorescence microscopy experiments. We waited 24 hours for the complete evaporation of distilled water before examining each sample [54].

The practices of SAM performed in the AI method and absorption spectra of QDs obtained from Avantes spectrometer with AvaSoft software at the room temperature. Colloidal QDs inside glass tubes were illuminated from above by a halogen lamp and a single mode fiber was used to collect light and then the absorption spectra of QDs were determined by the spectrometer as shown in Figure 5.1.

Firstly, the signals in scope mode checked whether they were saturated or not. If the signal saturated, integration time altered. Signals in the dark saved, then the halogen lamp turned on. The empty glass tube placed and its absorption spectra gained as a reference. Finally, colloidal QDs in glass tubes positioned, and their absorption spectra collected. Absorption, A, was calculated as;

$$A = -\log \frac{S_{sample} - S_{dark}}{S_{reference} - S_{dark}} \tag{5.1}$$

where S_{sample}, are the signals from the samples, S_{dark} are the signals collected in the

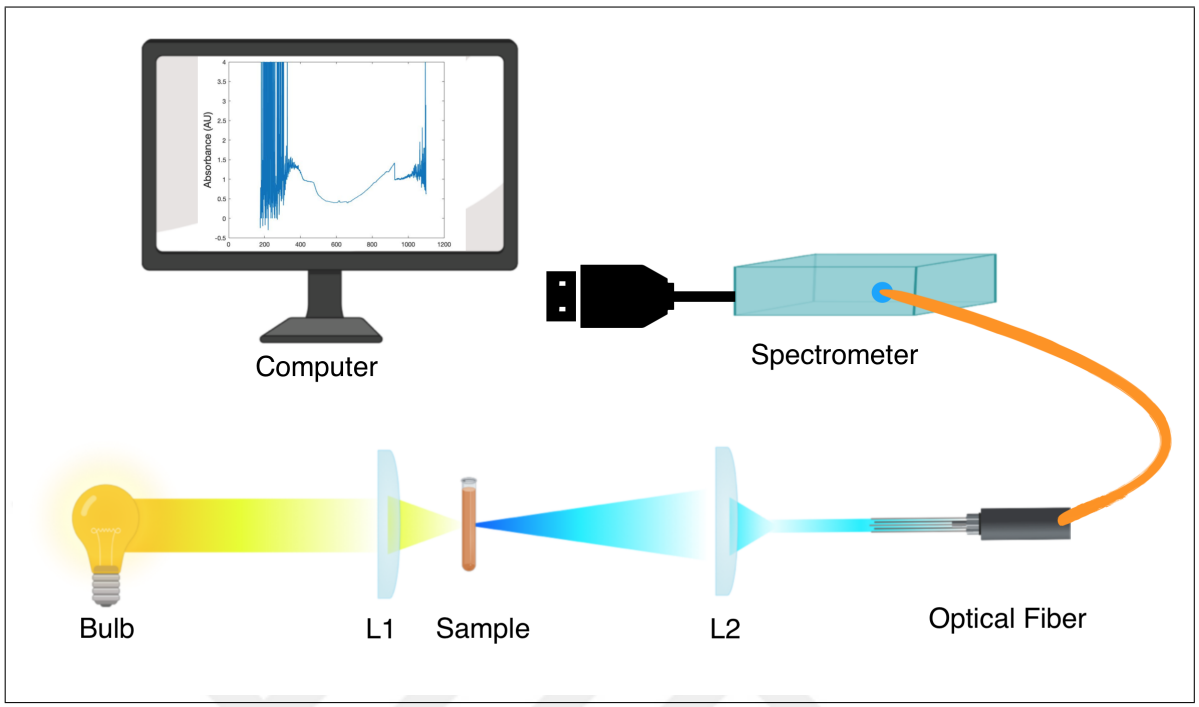

Figure 5.1. Ultraviolet–visible spectroscopy setup. It consists of a spectrometer, a halogen lamp, a single mode fiber, a sample holder and computer.

dark, and $S_{reference}$ are signals from the empty glass tube, respectively.

Zeiss Axio Observer 7 inverted fluorescence microscope was used to obtain the photoluminescence spectra of QD aggregates. The experiments were performed at the room temperature. The microscope has a focus controller, LED light sources of wavelengths of 385 nm, 430 nm, 475 nm, 511 nm, 590 nm, and 630 nm, carbon-dioxide (CO_2) module, five different objectives with 5x, 10x, 20x, 40x, and 63x magnification and two filters. We chose 40x magnification for the observations, and the resolution was 0.56 μm with this objective.

5.2. Results

Acoustic impedance maps of Figure 5.2, Figure 5.3 , Figure 5.4, and Figure 5.5, obtained by examining the reflected ultrasound signals from the surfaces of water and the specimens, in a scanning range of 4.8 mm x 4.8 mm with 300 x 300 sampling spots. The distilled water of acoustic impedance of 1.5 MRayl is chosen as reference matter, and similar droplet appearances on the right side of the maps refer to water. The scale

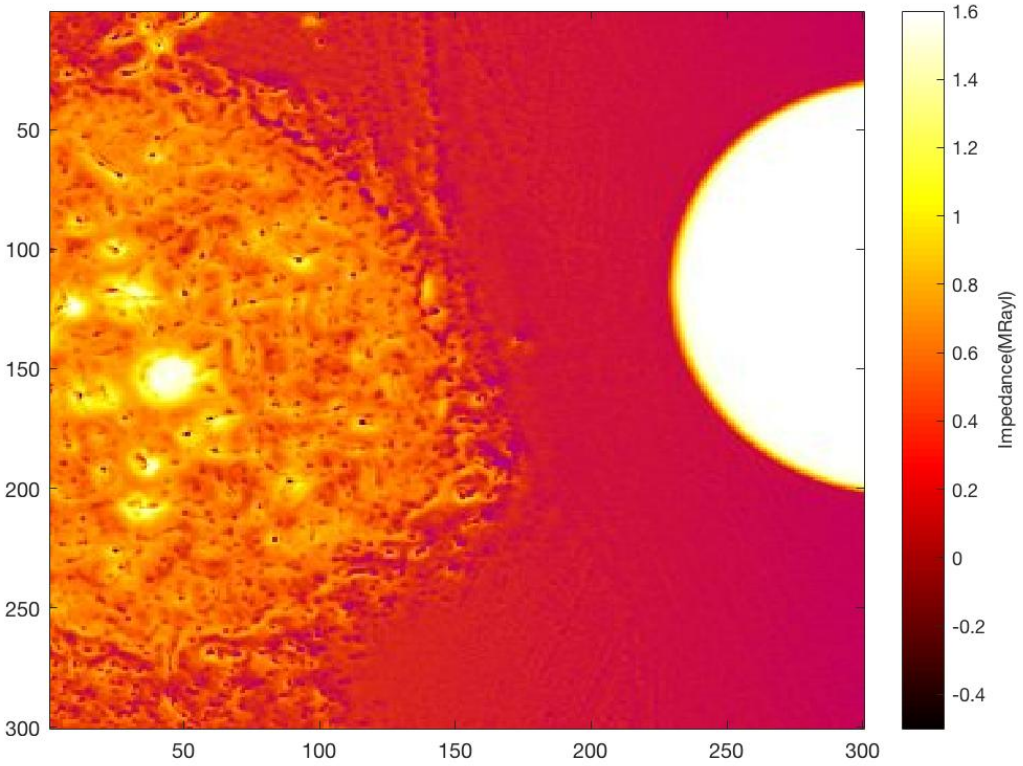

Figure 5.2. Acoustic maps of PbS QD aggregates.

bar of the acoustic impedance image of each QD aggregate is adapted to concern the most beneficial images presenting the QD aggregate distributions.

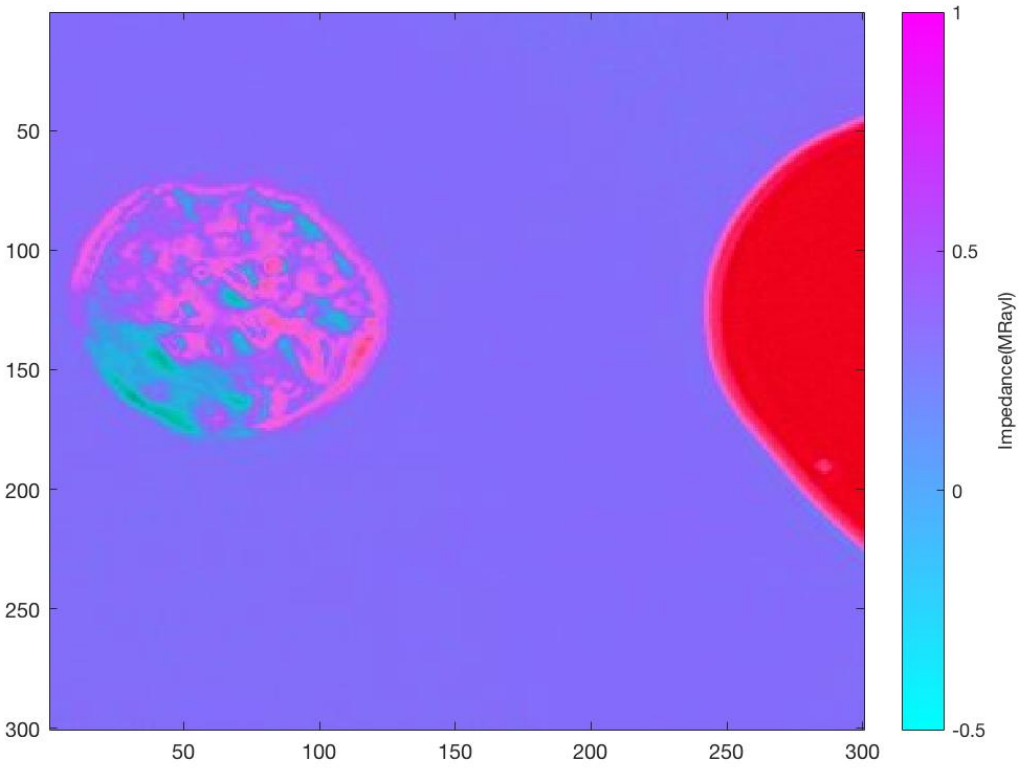

Figure 5.3. Acoustic maps of CdTe/CdS (green) QD aggregates.

Table 5.1. Acoustic Impedance Values of QD aggregates

QD	Mean Value (MRayl)	Standard Deviation (MRayl)
PbS	1.024	0.464
CdTe/CdS (green)	0.677	0.164
CdTe/CdS (orange)	0.865	0.469
Graphene	1.704	0.094

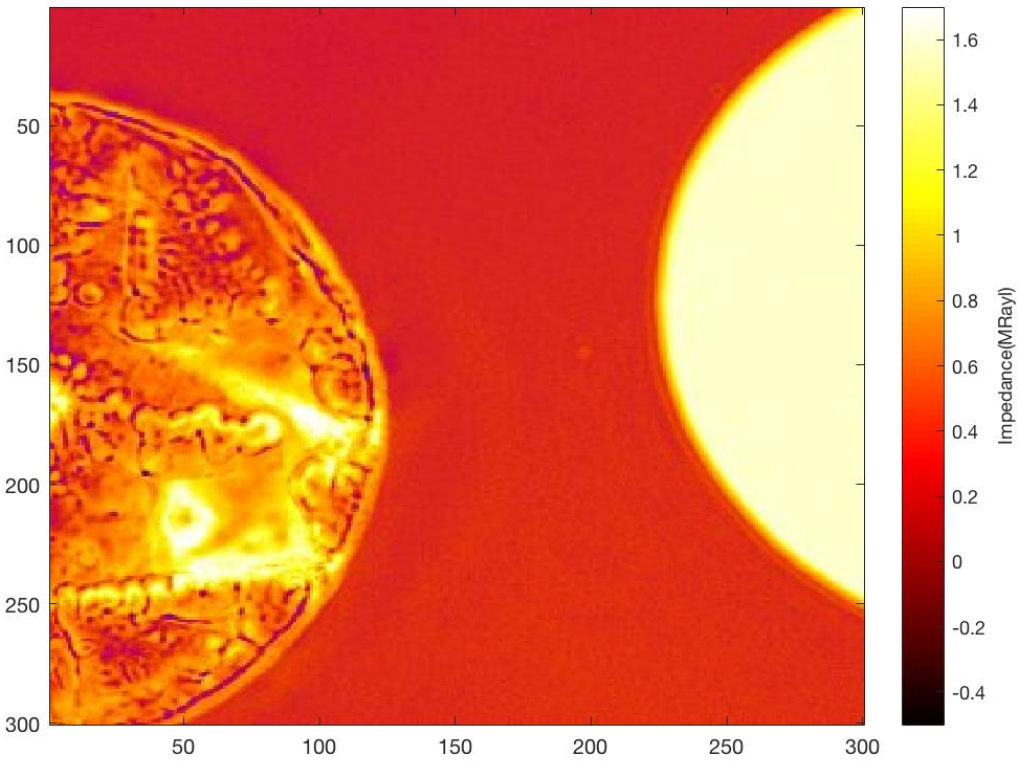

Figure 5.4. Acoustic maps of CdTe/CdS (orange) QD aggregates.

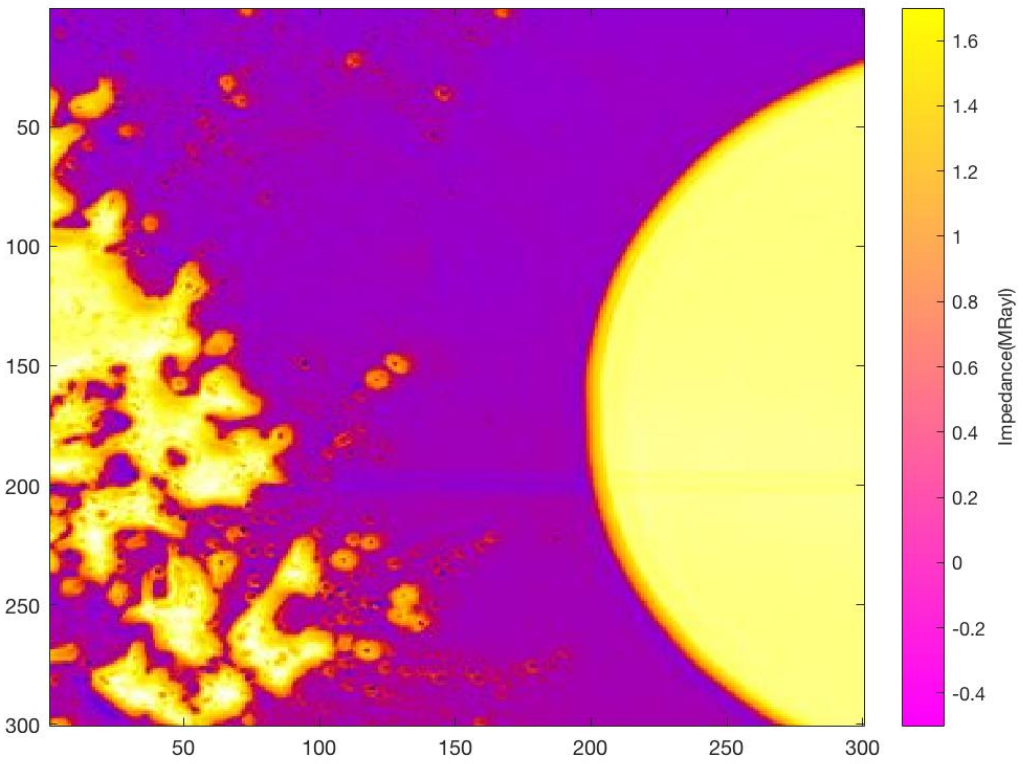

Figure 5.5. Acoustic maps of GQD aggregates.

Figure 5.6 indicates the absorption spectra of PbS, CdTe/CdS (green), CdTe/CdS (orange) and graphene QDs. The excitation wavelength for each QD for fluorescence microscopy was determined by these absorption spectra.

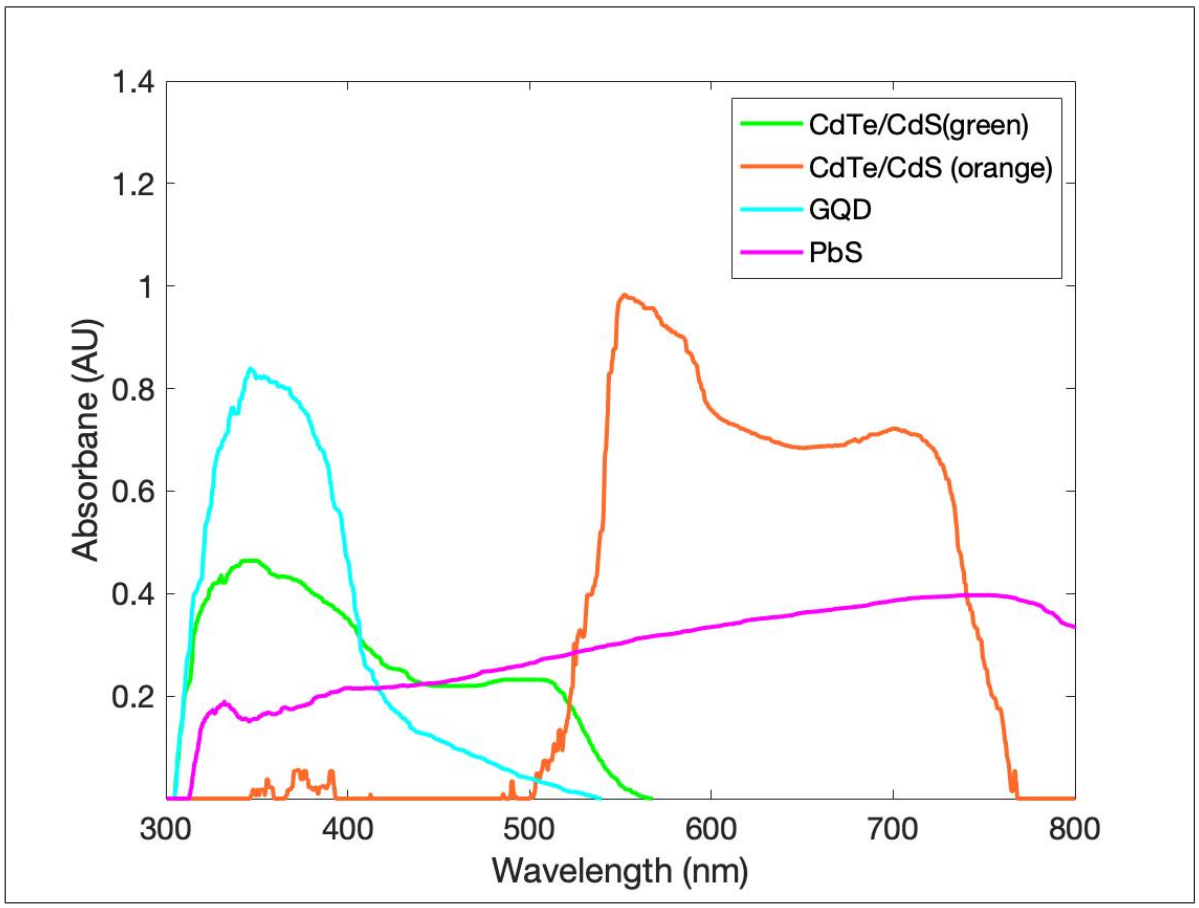

Figure 5.6. Characterization of QDs using ultraviolet–visible spectroscopy.

Photoluminescence image of PbS QD aggregates, obtained with excitation at 544 nm, is shown in Figure 5.7. For CdTe/CDS (green) QD aggregates excitation was at 430 nm and Figure 5.8 was obtained. Similarly, for CdTe/CDS (orange) QD aggregates, excitation was at 546 nm and Figure 5.9 was obtained. Finally, a photoluminescence image of graphene QD aggregates was obtained with excitation at 350 nm, as shown in Figure 5.10.

5.3. Discussion

We have confirmed that SAM can monitor the morphological and mechanical properties of QD aggregates by measuring the acoustic impedance values. Table 5.1

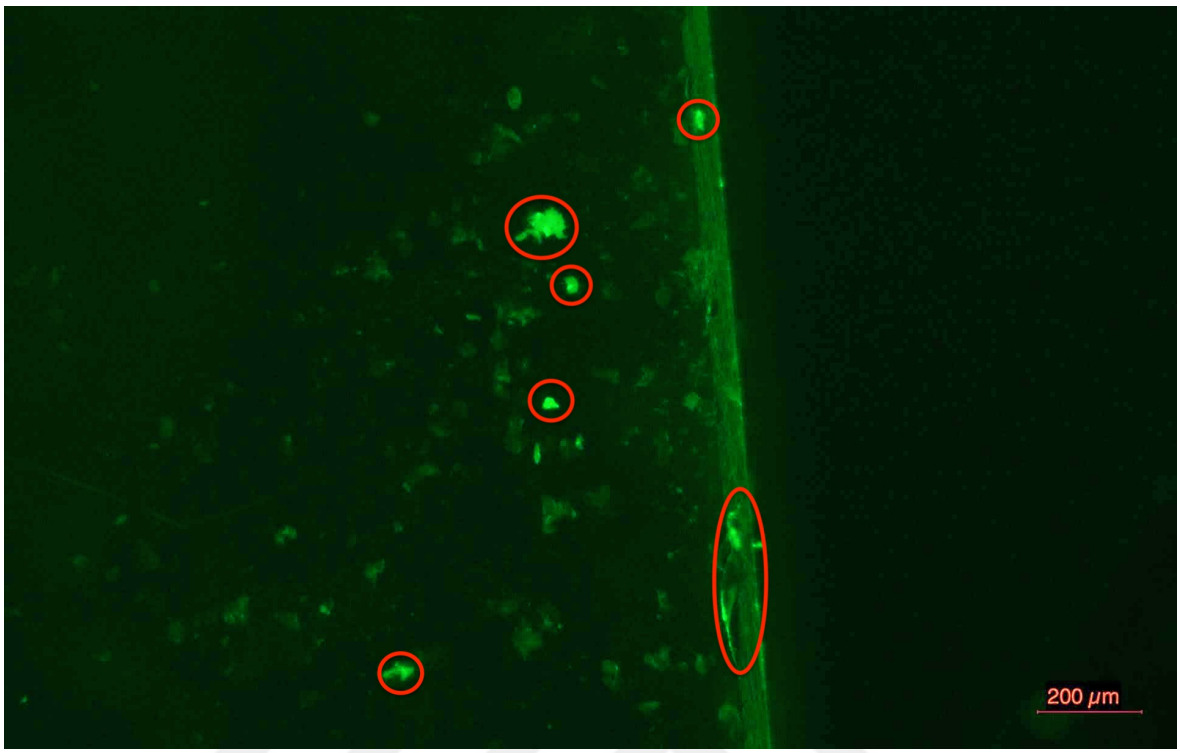

Figure 5.7. PbS QD aggregates excited with 544 nm. The intense aggregations were demonstrated in the circles.

reveals the average acoustic impedance and the standard deviation values of QD aggregates. Each type of QDs's mean acoustic impedance and standard deviation values calculated. The acoustic impedance value of PbS QD aggregates is 1.024 ± 0.464 MRayl. The standard deviation is great, since, the acoustic impedance values are directly proportionate to the amounts of the aggregates, which had utterly distinct values after the complete evaporation of distilled water of the PbS colloidal suspension.

The acoustic impedance values of CdTe/CdS (green) and CdTe/CdS (orange) QD aggregates are 0.677 ± 0.164 MRayl and 0.865 ± 0.469 MRayl, respectively. Standard deviation is higher for CdTe/CdS (orange) QD aggregates, since the formed aggregates were heterogenous. The acoustic impedance of graphene aggregates is 1.704 ± 0.094 MRayl with the most small standard deviation since the formed aggregates had alike volumes. SAM can obtain 2-D morphology and acoustic impedance charts of the specimen. Therefore, we were unable to measure the volumes of the aggregates and

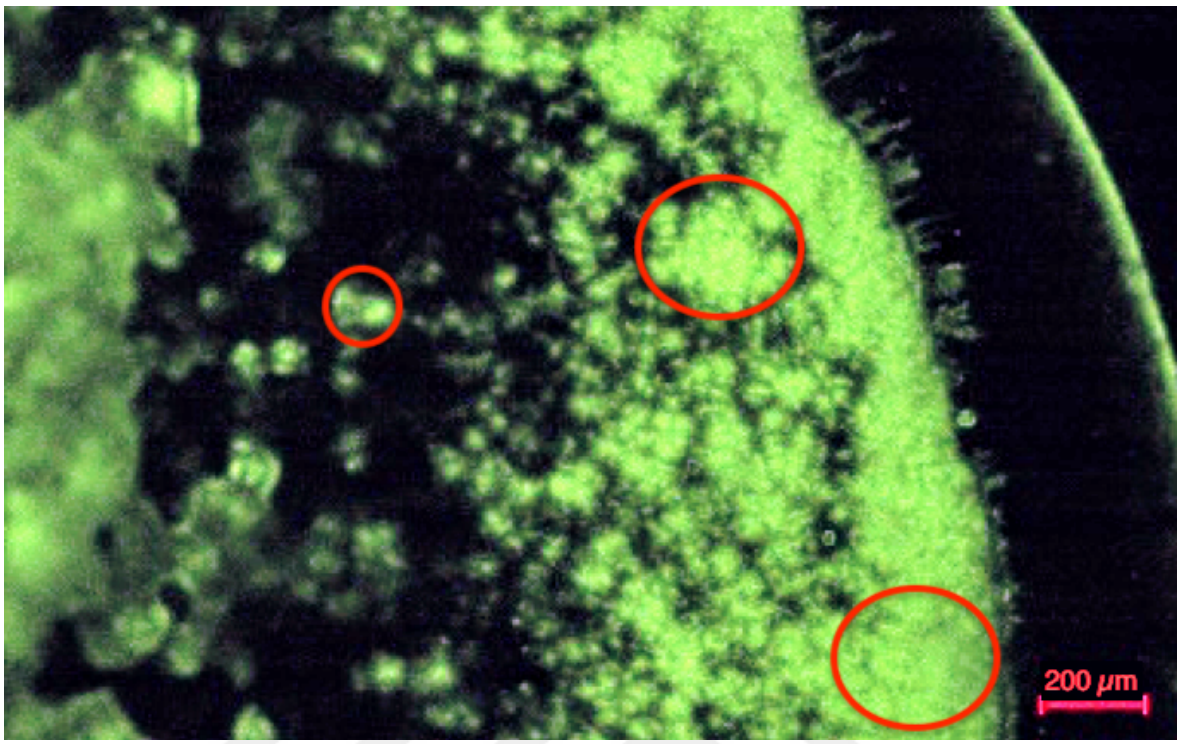

Figure 5.8. CdTe/CdS (green) QD aggregates excited with 430 nm. The intense aggregations were demonstrated in the circles.

found a similarity between acoustic impedance value and the volume of the aggregate.

The success of SAM in monitoring the QD aggregates is promising for the diagnosis of patients with potentially vulnareble plaques or tumors *in vivo*. The concentration and motion of macrophages contribute data about the growth of atherosclerotic plaques and gold nanoparticles are popularly used as contrast agents to image macrophages [55]. Furthermore, macrophage infiltration is a sign of cancer progression [56] and detection of macrophages by coloring them with QDs is significant [57,58]. A model of ultrasound stiffness checker was developed and used for the examination of human teeth [59]. Similar probe can also be used in operations to determine the boundaries of the diseased regions, which are stained by QDs, and therefore, provide physicians a more solid accuracy in their decisions. QDs have trend to aggregate and as the intensity is increased, aggregate structure is more expected to be observed. Acoustic levitation and swarm aggregations of nanoparticles in water are extremely desirable for many applications,

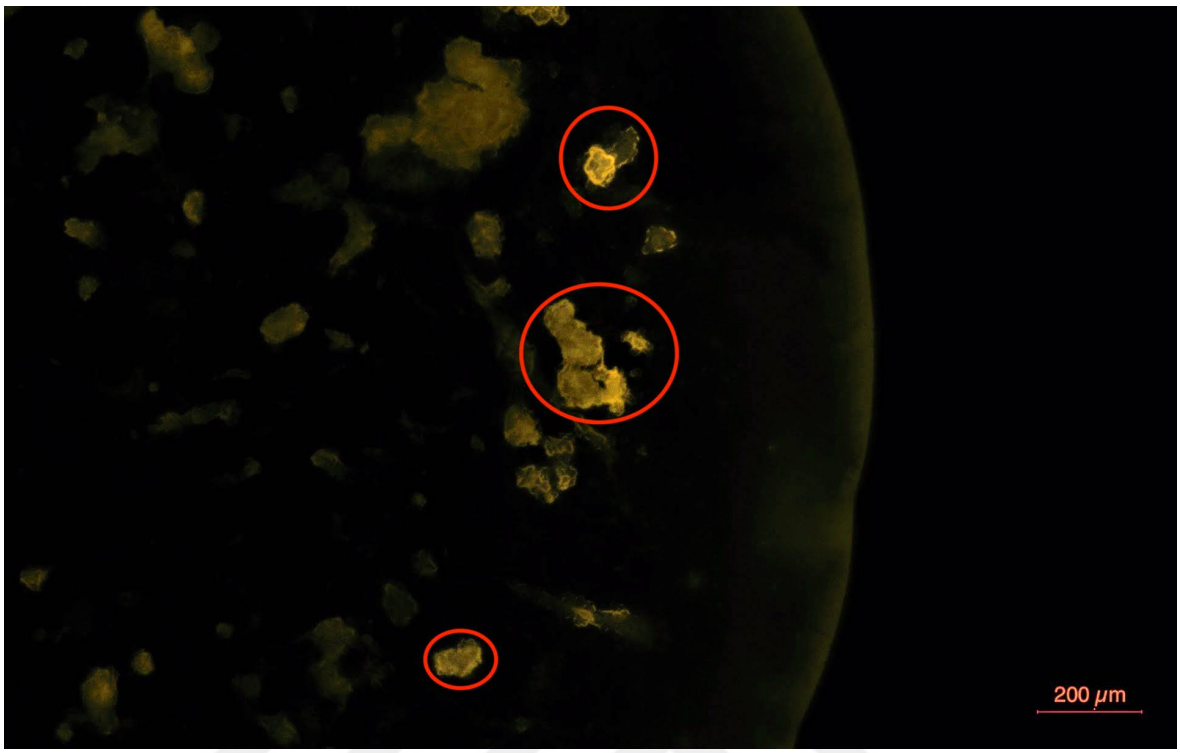

Figure 5.9. CdTe/CdS (orange) QD aggregates excitated with 546 nm. The intense aggregations were demonstrated in the circles.

uniquely in drug performance and cancer treatment, and can be checked by the applied voltage and the frequency of the acoustic field [60]. Imaging of these targeted QD aggregates provides detection and treatment of disorders. With a high frequency transducer, SAM can detect smaller aggregates or even individual QDs.

2D projections, as in Figures 5.2, 5.3, 5.4 and 5.5 received with micrometer resolution, and indicate the capacity of SAM as a suitable imaging modality for monitoring QD aggregates. Absolutely, graphene-based QDs are biocompatible in the human anatomy, can be used in clinical treatments [61]. To approve the advance of SAM, PbS, CdTe/CdS (green) and CdTe/CdS (orange) QDs represented in this research. They are poisonous and cannot be applied in clinics. The functionalized quantum dots would be plentifully steady and profoundly attached within the targeted part of the body. Hence, they have excellent aptitude in disease discovery. In addition to being excellent fluorescent probes providing high-resolution imaging, they can also be used in curative

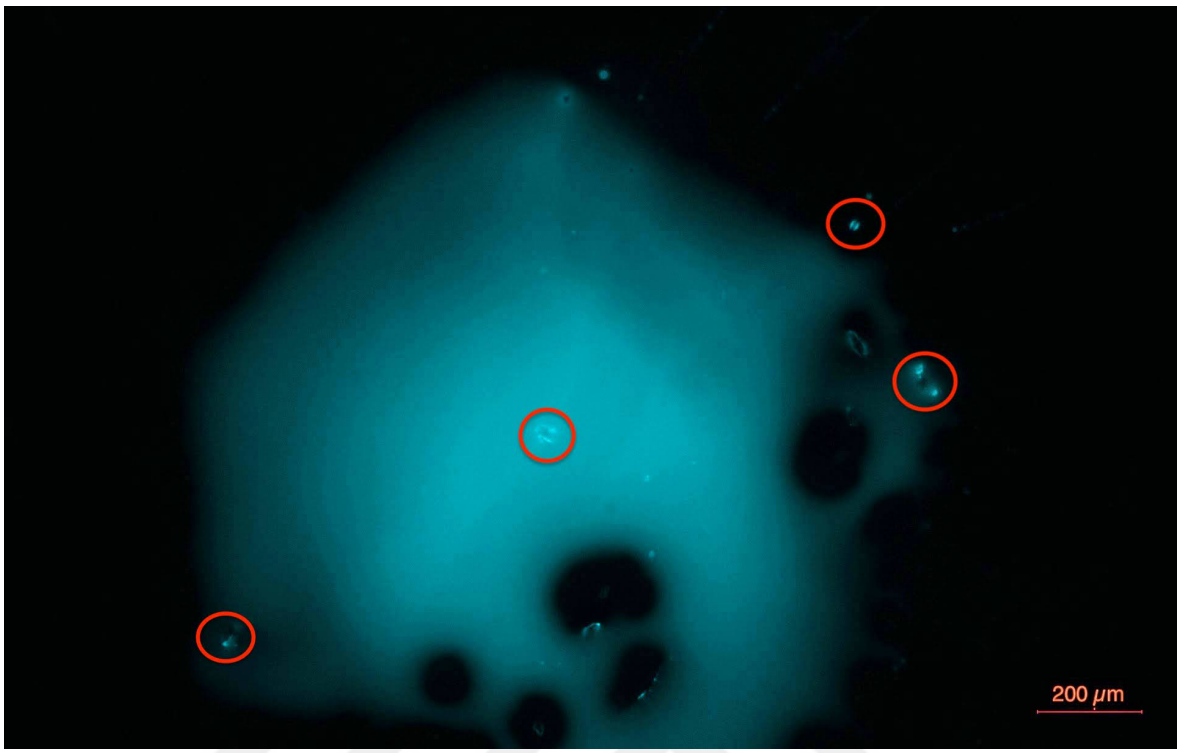

Figure 5.10. GQD aggregates excited with 350 nm. The intense aggregations were demonstrated in the circles.

applications [62].

Conventional fluorophores mostly show weak or annihilated fluorescence as a result of aggregation-caused quenching, which leads to weak or nearly no emission in aggregate state and inhibits their biological applications [63]. Fluorophores with aggregation-induced emission have great potential in long-term bioimaging since they have excellent photostability and therefore, are widely used in fluorescence and photoacoustic microscopy [64–66]. For SAM, the photostability of the fluorophores is not an issue, since it measures the acoustic impedance value of the aggregates, which has nothing to do with fluorescence and, therefore, will be a valid technique for the detection of any fluorophore. QD aggregates have not been evaluated with SAM so far and thus our study will be preliminary.

Figure 5.6 exposes the characterization of QDs using ultraviolet-visible spectroscopy, which granted the greatest absorption values; therefore, the excitation wavelength values for the highest photoluminescence rates of QD aggregates. Figures 5.7, 5.8, 5.9 and 5.10 reveal the photoluminescence images of QD aggregates taken with the excitation wavelengths determined in the absorption spectra. $40x$ magnification was chosen for the measurements, and the resolution of the images was 0.56 μm with this objective. Higher resolution in optical microscopy resulted in more precise images compared to the SAM images of resolution of 20μ m. The resolution of the SAM images can be adjusted with a higher frequency transducer than an 80 MHz transducer. In Figure 5.7, we recognize PbS QD aggregates of shifting dimensions. SAM also monitors these aggregates as in Figure 5.2, which presents agreement to Figure 5.7. In Figure 5.8, we witness CdTe/CdS (green) QD aggregates of smooth dimensions. These aggregates are also seen by SAM as exhibited in Figure 5.3, which reveals correspondence to Figure 5.8. In Figure 5.9, we screen CdTe/CdS (orange) QD aggregates of non-uniform dimensions. The image taken by SAM in Figure 5.4 and the Figure 5.9 obtained by optical microscopy have connection. As can be seen in Figure 5.10, graphene QD aggregates have considerably uniform distributions, also proved by the SAM image shown in Figure 5.5. Various aggregate configurations are perceived since different chemical contents, and manufacturing techniques were used for QD structures. The similarity of the images captured by both modalities supported SAM as an alternative method in biological imaging and drug delivery domains.

In this section, we judge the potential of SAM in the characterization and detection of QD aggregates for the first time. Acoustic impedance pictures of the QD aggregates display separate patterns and values for different sorts of quantum dots resulting from arbitrary formations of aggregates. Consequently, we can state that SAM facilitates the early diagnosis and the follow-up of the treatment of a specific condition since it can simultaneously gain morphological and chemical information.

6. DETERMINATION OF MODIFICATIONS IN RAT LIVER TISSUE DUE TO PHTHALATE UPTAKE BY SCANNING ACOUSTIC MICROSCOPY, AND RAMAN SPECTROSCOPY

6.1. Materials and Methods

Plasticizers are the chemical elements that transform the physical features of the substances. Phthalates esters are generally used as plasticizers, especially in polyvinyl chloride (PVC), to modify the production's elasticity and durability. The phthalates are environmental pollutants and toxic composites, separate the environment over time because their chemical bonds to the plastics are weak. Accordingly, humans and animals are subjected to them by breathing, digesting, or during medical processes, and the side effects of the phthalate esters are observed [67]. The deterioration of the phthalic acid esters depends on exposure time, the concentration of the phthalates, and the living creatures' lifetime. Animal studies explained that clustering DEHP in the tissues creates long-term toxicity, lowering fertility and fetus mortality [68]. DEHP-induced tumor formation in rodent liver was assigned to be arising the pathway of continued low-level oxidative stress, collection of DNA damage, and the appearance of the pre-neoplastic nodules [69]. However, there is no study of DEHP-induced liver cancer formation in humans. Human-based studies unveiled increasing allergic disorders and asthma due to the modification of the immune system [70].

The Ethical Committee approved this study of Istanbul University (Number: 2013/138). Healthy adult male and female Sprague Dawley rats were provided by the Laboratory Animal Center at Istanbul University. They were accommodated in a cage in a controlled atmosphere at $22 \pm 3°C$ and a relative humidity level of 50-60 % with a 12/12 h light/dark period. There were four groups composed of pregnant rats of control, low dose prenatal that given a low dose of DEHP and DBP dissolved in corn oil, and high dose prenatal that given a high dose of DEHP, dissolved in corn

oil, together with their female offspring rodents. Edible corn oil was given to rats by intragastric administration in the control group. Low and high intragastric doses were 61 μg/kg/day, and the low and high fetal groups delivered 61 mg/kg/day, respectively, and these doses were delivered prenatal groups at the same time of each day from the sixth to the nineteenth day of the pregnancy. All mother rats were anesthetized using ether and cervical dislocation in the twentieth day of pregnancy. The liver tissues were carefully extracted, cleaned, and fixed in 4 % paraformaldehyde (PFA).

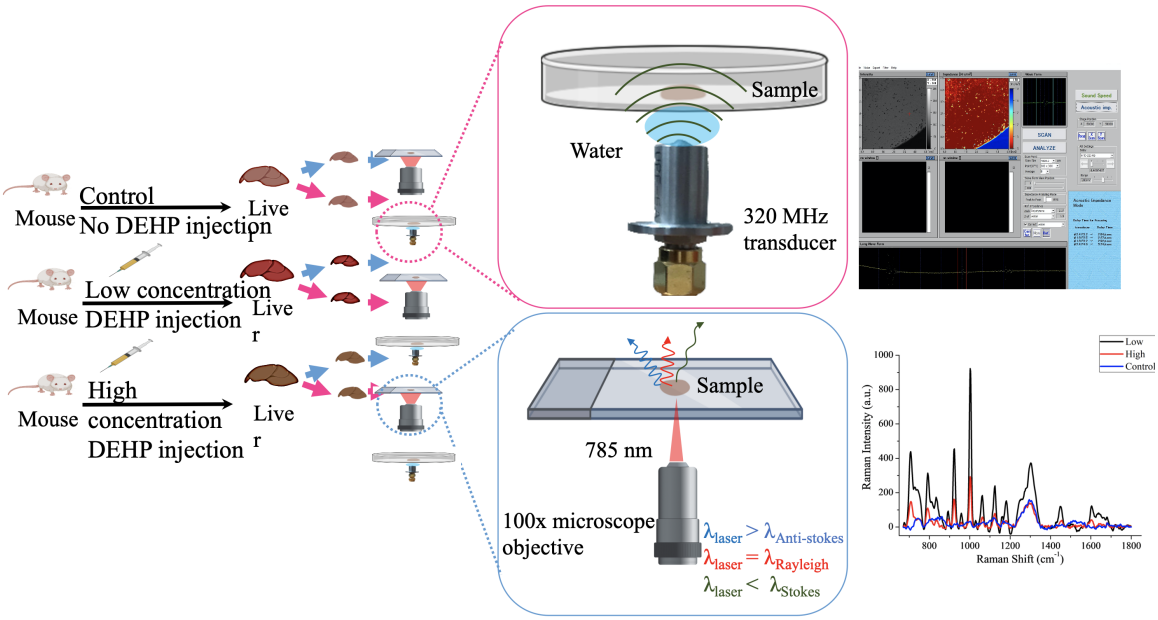

Figure 6.1. A brief explanation of SAM and Raman spectroscopy procedure

Raman spectra of the liver tissues taken through scanning each tissue. For each sample, both from parent and offspring, 440 spectra attained, which delivered about 5 seconds. The tissues were scanned with the step sizes of 50 m to prevent bias on signal quality due to the initial selection of region because they are inhomogeneous.

The liver tissues sliced cross-sectionally for SAM studies. The SAM images, in AI mode, were constructed by collecting the reflections of ultrasound signals both from the reference and front surfaces of the slices shown in Figure 6.1.

6.2. Results

In Table 6.2, the average of the acoustic impedance value of mother rats and their female offspring rats' are provided. Tissue specimens were distinguished easily, considering tissues that relate to the mother rats exposed to DEHP and DBP are considerably rigid, and therefore have higher acoustic impedance values. In other words, the fluctuations in acoustic impedance values are due to the change in the tissues' elastic properties. On the other hand, average acoustic impedance values of liver tissues of offspring rats of control and DEHP and DBP exposed parent rats do not deviate significantly. Figure 6.2 is an example of the images captured in AI mode and displays the acoustic impedance distribution of the liver sample taken from an offspring rat of the control mother rodent.

Tissue	**Control Acoustic Impedance (MRayl)**	**DBP(Low) Acoustic Impedance (MRayl)**	**DEHP (Low) Acoustic Impedance (MRayl)**	**DEHP (High) Acoustic Impedance (MRayl)**
Parent	1.33 ± 0.35	1.71 ± 0.06	1.95 ± 0.15	1.54 ± 0.06
Offspring	1.70 ± 0.09	1.63 ± 0.05	1.77 ± 0.08	1.69 ± 0.06

Table 6.1. Acoustic impedance values of liver tissues of the pregnant control rat and pregnant rats exposed to different concentrations of phthalates of DEHP and DBP and average acoustic impedance values of tissues of their offspring rats. Low is for a 61 μg/kg/day and high for a concentration of 61 mg/kg/day, applied to these rats from the sixth to the nineteenth day of pregnancy.

The average Raman spectra of all the tissues were analyzed and revealed in Figure 6.3. The scans were used to confirm the reproducibility of the signals. As we see in the insets of Figure 6.3, the spectra are highly reproducible. The diversity in the peak intensities was determined by estimating their average and standard deviation values. Table 6.2 shows that signal intensity values of the liver tissue of the mother rat exposed to low dose DEHP are more significant than those of tissues of control mother rat and mother rat exposed to high dose, which is compatible with results of SAM. Furthermore, it is apparent in Table 4 that the Raman spectra of mother rats' tissues have some missing and shifted peaks when compared to the spectra of offspring rats' tissues.

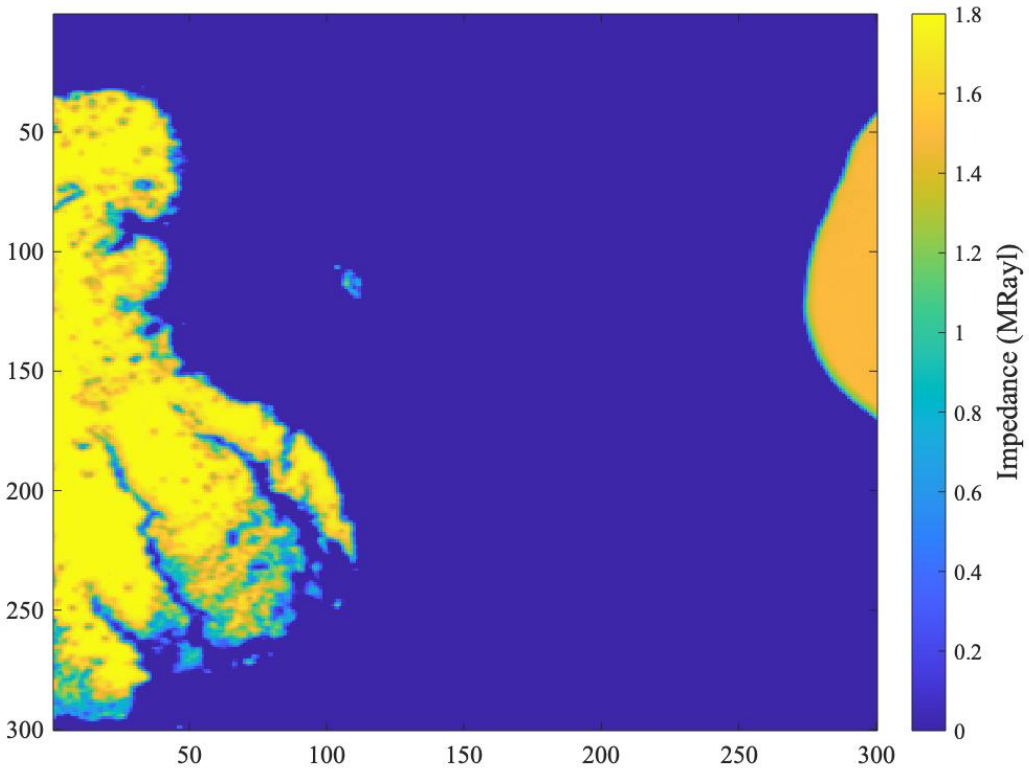

Figure 6.2. SAM image of the liver tissue of an offspring rat of the control mother rat. Scanning area is 4.8 mm x 4.8 mm.

Mother samples have higher peak intensities at the common peaks, 1002, 1060, 1126, 1248 cm^{-1}, that indicate the outcome of DEHP on tissue protein, and lipid/collagen formation is drastically higher for offspring rat samples. On the other hand, the averaged signal intensity of the rodents' tissues exposed to low dose is lower than that of the tissues of the rats exposed to high doses only at 1002 cm−1, which is tentatively assigned to ring breathing mode of Phenylalanine amino acid. Parent tissues have missing peaks for nucleic acids, 742, 792, 834, 1182 cm^{-1}, lipids, 1300 cm^{-1}, and 1460 cm^{-1}, and protein-related bands, 1604, and 1640 cm^{-1}, while the peaks at 738, C-S vibration, 815, 1311, 1437 cm^{-1}, lipid/collagen, are missing for offspring rat samples.

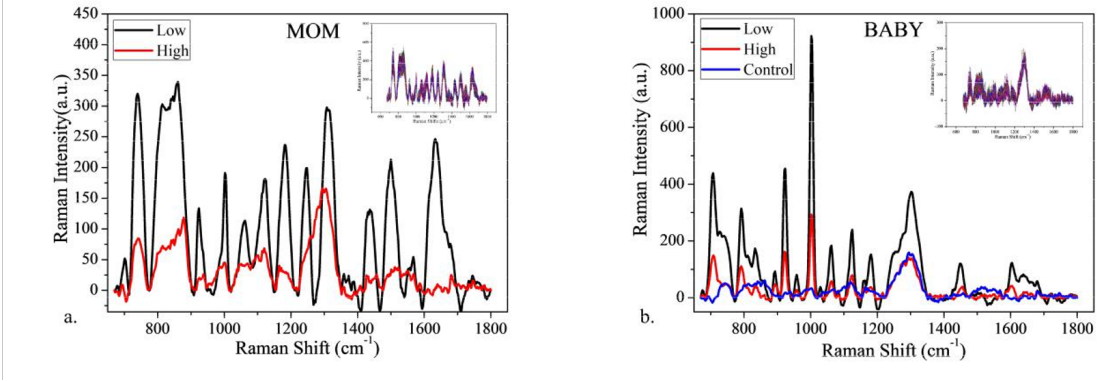

Figure 6.3. a. Averaged Raman spectra of the tissues of mother rats exposed of high and low doses of DEHP. b. Averaged spectra of the tissues of offspring rats.

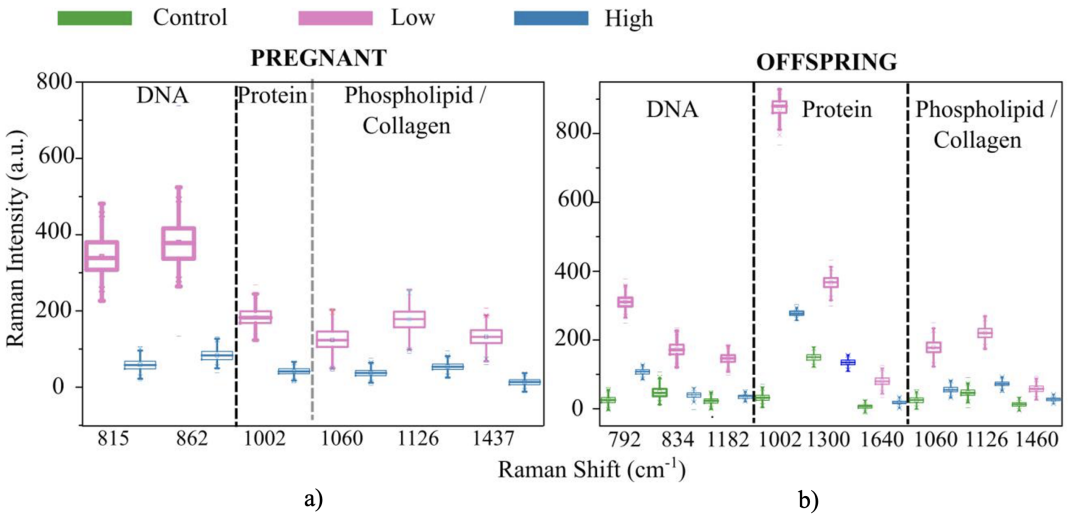

Figure 6.4. a. Box plots to compare the molecular responses of low and high dose exposed tissues from pregnant samples. b. Molecular comparison for the offspring rats.

6.3. Discussion

Phthalates induce damages in reproductive organs in animals and also in humans with high concentration exposure. SAM can show the impact within samples, by estimating acoustic impedance values of liver tissues of parent and offspring rats. As can be seen in Table 6.2, acoustic impedance values of liver tissues of the low dose of DEHP exposed mother rat is higher than those of tissues of control mother and the high dose of DEHP exposed parent rat. Each acoustic impedance value of offspring rats in Table 6.2 is the average of offspring rats of the same parent. Tissues of offspring rats of DBP and DEHP exposed mother rats have similar acoustic impedance values when correlated to those of offspring rats of the control mother, and this similarity may be due to a rise in some element levels but a decrease in others. Levels of essential elements and minerals have active roles in enzyme expression, and synthesis and phthalates have been shown to decrease steroidogenic enzymes' levels due to oxidative stress targeting the endocrine system. [86–96]

Raman spectroscopy, peak intensities are placed as low, high, and dose-free exposure tissues for both parent and offspring rats, as displayed in Figure 6.4. In the offspring group, most of the peaks altered are related to nucleic acids. [97] It has been revealed that the damage resulting in DNA generates conformational differences. Also, some of the DNA linked peaks increment; others have the reverse trend because of reactive oxidative species. [98] A shred of evidence stating that the DEHP accommodation drives to DNA damage in sperm cells was found, confirming the previous result. [99] It was also demonstrated that the collagen and glycogen formation of the tissues are altered conditioned by the increase of phthalate esters [100], which can be observed from the CH2/CH3 bending and twisting modes in the Raman spectra. This article also explains the short term effects in lipid structure, which are apparent in the C-C skeletal stretch related (non-collagen) peaks of the rodent liver tissue spectra [101] that the storage of DEHP in the liver produces peroxisomes, which increases the number of proteins and phospholipids. The increase in the peaks at $1002, 1604$, and $1640\ cm^{-1}$ is parallel to these findings.

We proposed to study the impact of DEHP and DBP on liver tissues of both mother rats and their offspring female rats by SAM, RS. Exposure doses of $61\mu g/kg/day$ and $61mg/kg/day$ are studied to evaluate dose impact on the liver. SAM is capable of obtaining a micrometer resolution monitoring and acoustic impedance distributions, and consequently, it is successful in predicting structural and functional transformations induced by DBP and DEHP exposure. RS results support molecular changes in liver tissues. Ultimately, we can say that phthalates affect rat liver modifications, which can be recognized by SAM, and RS.

Table 6.2. Comparison of the averaged signal intensities of tissues excised from pregnant and offspring rat tissues.

	PARENT		***CHILD***				
	Low	**High**	**Control**	**Low**	**High**	**Assignment**	**Ref**
	Avg ± Std	**Avg ± Std**	**Avg ± Std**	**Avg ± Std**	**Avg ± Std**		
738	369,94 ± 55,43	64,48 ± 16,35	-	-	-	C-S stretch	[71]
742	-	-	49,77 ± 17,17	218,40 ±21,54	45,47 ± 9,61	T (DNA)	[72]
792	-	**-**	25,74 ± 11,87	218,60 ± 19,18	107,47 ± 9,17	DNA	[73]
815	342,42 ± 54,60	58,94 ± 15,31	-	-	-	Pro, Tyro, DNA	[74]
834	-	-	48,03 ± 16,17	212,03 ± 20,92	39,97 ± 9,65	O-P-O , Tyr	[72]
1002	183,29 ± 22,84	41,82 ± 9,65	32,53 ± 10,88	206,56 ±27,93	277,93 ± 7,91	Phe	[74, 75]
1060	124,04 ± 30,94	37,56 ± 10,71	24,73 ± 9,64	139,77 ± 20,59	55,34 ± 9,77	C-C skeletal stretching	[76]
1126	178,33 ± 30,98	53,80 ± 10,55	46,82 ± 11,11	135,49 ±17,47	72,08 ± 7,92	n(C-C) (lipid)	[74]
1182	-	-	22,70 ± 9,32	124,88 ± 14,75	35,53 ± 6,51	[HTML]211E1E C, G	[77]
1248	200,20 ± 32,78	62,49 ± 10,62	59,24 ± 15,51	121,80 ± 16,36	58,70 ± 7,96	Amide III (collagen), G, C	[75, 77]
1300	-	-	149,73 ± 10,71	116,27 ± 19,36	134,46 ± 9,99	(CH2)n- in-plane (lipid)	[78–80]
1311	309,56 ± 30,97	144,53 ± 11,31	-	-	-	Lipid/ collagen	[74]
1437	131,87 ± 24,28	13,26 ± 9,75	-	-	-	CH2 (lipids in normal tissue)	[81–83]
1460	-	-	12,90 ±7,01	66,22 ± 11,87	27,44 ± 6,01	CH2/CH3 deformation (lipids, DNA)	[74, 77]
1604	-	-	-4,66 ± 6,94	85,01 ± 13,14	40,61 ± 6,09	C-C in-plane bending (Phe &Tyr)	[82, 84]
1640	-	-	6,15 ± 6,96	67,50 ± 13,98	17,66 ± 6,74	Amide I	[85]

7. CONCLUSION

The thesis has explained the content consisting of two achievements. In this chapter, the conclusion is described based on each achievement in the following.

The first achievement was reported in chapter 5. SAM for measuring the acoustic impedance of various QDs was proposed. The potential of SAM in the characterization and detection of QD aggregates was demonstrated for the first time. Different acoustic impedance values of QD aggregates observed as a result of random accumulation. Consequently, it could be stated that SAM enabled the early diagnosis and the follow up of the treatment of a precise disease since it simultaneously acquired morphological and chemical information.

The second achievement was explained in chapter 6. SAM for determining the acoustic impedance of liver tissues from the rats exposed to phthalates was revealed. SAM was able to monitor the impact within samples, by determining acoustic impedance values of liver tissues of mother and offspring rats. The variation of acoustic impedance values of liver tissues was observed due to different concentrations of the plasticizers. In the RS, experiment, peak intensities were classified. In the offspring group, most of the altered peaks were linked to nucleic acids. The collagen and the glycogen structure pf the liver tissues were also affected by the phthalate esters. C - C skeletal stretch peaks were observed, which affects the lipid structure.

SAM can successfully detect the structure of the cell. It will be an excellent opportunity to investigate the cell's biomechanical properties with nanoparticles. If the acoustic impedance and sound speed are known, the density of the cell structure can be measured. Thus, it can be differentiated cells from each other according to the number of nanoparticles they take. For future applications, this technique can be used for medical necessities.

REFERENCES

1. Pietzsch, J., "An illuminating accident", `https://www.nobelprize.org/prizes/physics/1901/speedread/`, accessed: 16.09.2020.

2. Demirkan, I., *Mechanical Characterization of Cells and Tissues by Scanning Acoustic Microscopy and Optical Tweezer*, Ph.D. Thesis, Bogazici University, 2020.

3. Shung, K. K., *Diagnostic ultrasound: Imaging and blood flow measurements*, CRC Press, 2011.

4. Carovac, A., F. Smajlovic and D. Junuzovic, "Application of Ultrasound in Medicine", *Acta Informatica Medica*, Vol. 19, No. 3, p. 168–171, 2011.

5. Graham, K. C., Wirtzfeld, L. A., L. T. MacKenzie, C. O. Postenka, A. C. Groom, I. C. MacDonald, A. Fenster, J. C. Lacefield and A. F. Chambers, "Three-Dimensional High-Frequency Ultrasound Imaging for Longitudinal Evaluation of Liver Metastases in Preclinical Models", *Cancer Research*, Vol. 65, No. 12, 2005.

6. Czarnota, G., M. C. Kolios, J. Abraham, M. Portnoy, F. Ottensmeyer, J. Hunt and M. Sherar, "Ultrasound imaging of apoptosis: high-resolution non-invasive monitoring of programmed cell death in vitro, in situ and in vivo", *British Journal of Cancer*, Vol. 81, No. 3, 1999.

7. Dijkgraaf, S., "Spallanzani's Unpublished Experiments on the SensoryBasis of Object Perceptionin Bats", *History of Science and Society*, Vol. 51, No. 1, pp. 9–20, 2014.

8. Manbachi, A. and R. S. Cobbold, "Development and application of piezoelectric materials for ultrasound generation and detection", *Ultrasound*, Vol. 19, No. 4, pp. 1–10, 2011.

9. Lewiner, J., "Paul Langevin and the Birth of Ultrasonics", *Japanese Journal of Applied Physics*, Vol. 30, 1991.

10. David, J. and N. Cheeke, *Fundamentals and Applications of Ultrasonic Waves*, CRC Press, Boca Raton,FL, USA, 2012.

11. Chilowsky, C. and P. Langevin", ""Production of Submarine Signals and the Location of the Submarine Objects"", , Oct 23 "1923", "https://patents.google.com/patent/US1471547A/en", "US Patent 1,471,547".

12. Lynnworth, L. C., "Industrial Applications of Ultrasound - A Review", *IEEE Transactions on Sonics and Ultrasonics*, Vol. 22, No. 2, pp. 71–100, 1975.

13. Jones, R. and I. Facaoaru, "Recommendations for testing concrete by the ultrasonic pulse method", *Materiaux et Construction, JUILLET–AOUT*, Vol. 2, p. 275–284, 1969.

14. Glover, G. H., "Overview of Functional Magnetic Resonance Imaging", *National Institute for Health*, Vol. 22, No. 2, pp. 133–139, 2011.

15. Hecht, E., *Optics*, Pierson, Edinburgh, England, 2017.

16. Bushberg, J. T., J. A. Seibert, E. M. L. Jr. and J. M. Boone, *The Essential Physics of Medical Imaging*, Lippincott Williams Wilkins, 2011.

17. Cox, B., *Acoustics for Ultrasound Imaging*, Ph.D. Thesis, 2013.

18. GUNAWAN, A. I., *A Study on Acoustic Impedance Microscopy for Biological and Medical Applications*, Ph.D. Thesis, Toyoshi University of Technology, 2015.

19. Briggs, A., "Acoustic microscopy-a summary", *Reports on Progress in Physics*, Vol. 55, No. 7, pp. 851–909, 1992.

20. Kobayashi, K., Y. Saijo and N. Hozumi, "Acoustic impedance microscopy for

biological tissue characterization", *Ultrasonics*, Vol. 54, No. 7, pp. 1922 – 1928, 2014.

21. Sherar, M. and F. Foster, "The design and fabrication of high frequency poly (vinylidene fluoride) transducers", *Ultrasonic imaging*, Vol. 11, No. 2, 1989.

22. Raman, C. and F.R.S, "A new radiation", *Indian Journal of Physics*, Vol. 2, pp. 387 – 398, 1928.

23. Pietzsch, J., "The Nobel Prize in Physics 1930", `https://www.nobelprize.org/prizes/physics/1930/summary/`, (accessed: 01.09.2016).

24. Casadio, F., C. Daher and L. Bellot-Gurlet, "Raman Spectroscopy of Cultural Heritage Materials: Overview of Applications and New Frontiersin Instrumentation, Sampling Modalities, and Data Processing", *Topics in Current Chemistry*, Vol. 374, No. 62, 2016.

25. Akhtar, R., J. Cruickshank, X. Zhao, B. Derby and T. Weber, "Applications of Raman Spectroscopy in Art and Archaeology", *Journal of Raman Spectroscopy*, Vol. 50, No. 2, pp. 137–142, 2019.

26. Lawson, E. E., B. W. Barry, A. C. Williams and H. G. M. Edwards, "Biomedical Applications of Raman Spectroscopy", *Journal of Raman Spectroscopy*, Vol. 28, pp. 111–117, 1997.

27. Ferraro John R. and, N. K. and B. C. W., *Introductory Raman Spectroscopy*, Elsevier, 2003.

28. Harrison, P., *Quantum Wells, Wires and Dots: Theoretical and Computational Physics of Semiconductor Nanoparticles*, John Wiley & Sons, Inc., 2005.

29. Miller, D., "Optoelectronic Applications of Quantum Wells", *Optics and Photonics News*, Vol. 1, No. 2, pp. 7–14, 1990.

30. Silberberg, Y., P. W. Smith and D. J. Eilenberger, "Passive Mode Locking of a Semiconductor Diode Laser", *Optics Letters*, Vol. 9, No. 11, pp. 507–509, 1984.

31. Bamham, K., I. Ballard, J. Barnes, J. Connolly, B. Kluftinger, J. Nelson, E. Tsui and A. Zachariou, "Quantum well solar cells", *Applied Surface Science*, Vol. 113, No. 114, pp. 722–733, 1997.

32. Kim, H., S. Beack, S. Han, M. Shin, T. Lee, Y. Park, K. S. Kim, A. K. Yetisen, S. H. Yun, W. Kwon and S. K. Hahn, "Multifunctional Photonic Nanomaterials for Diagnostic, Therapeutic, and Theranostic Applications", *Advanced Materials*, Vol. 30, No. 10, p. 1701460, 2018.

33. McHugh, K. J., L. Jing, A. M. Behrens, S. Jayawardena, W. Tang, R. L. M. Gao and A. Jaklenec, "Biocompatible Semiconductor Quantum Dots as Cancer Imaging Agents", *Advanced Materials*, Vol. 30, No. 18, p. 1706356, 2018.

34. Papagiannaros, A., J. Upponi, W. Hartner, D. Mongayt, T. Levchenko and V. Torchilin, "Quantum dot loaded immunomicelles for tumor imaging", *BMC Medical Imaging*, Vol. 10, No. 22, 2010.

35. Hu, J., D. H. Ortgies, R. A. Torres, N. Fernandez, L. Porto, E. Rodriguez, J. G. Sole, D. Jaque, F. Alfonso and F. Rivero, "Quantum Dots Emitting in the Third Biological Window as Bimodal Contrast Agents for Cardiovascular Imaging", *Advanced Functional Materials*, Vol. 27, No. 41, p. 1703276, 2017.

36. Ko, N. R., M. Nafiujjaman, J. S. Lee, H. N. Lim, Y. K. Lee and I. K. Kwon, "Graphene quantum dot-based theranostic agents for active targeting of breast cancer", *Royal Society of Chemistry Advances*, Vol. 7, No. 19, p. 11420, 2017.

37. Yamazaki, R., K. Ogasawara, M. Fujiwara, K. Kobayashi and Y. Saijo, "Macrophage with Gold Nanorod Visualized by Optical-Resolution and Acoustic-Resolution Photoacoustic Microscopes", *Conference Proceedings of IEEE Engineering in Medicine and Biology Society*, Vol. 2015, No. 41, pp. 2387–90, 2015.

38. Yang, K., S. Zhang, G. Zhang, X. Sun, S. Lee and Z. Liu, "Graphene in Mice: Ultrahigh In Vivo Tumor Uptake and Efficient Photothermal Therapy", *Nano Letters*, Vol. 10, pp. 3318–3323, 2010.

39. Wang, H., R. Revia, K. Wang, R. J. Kant, Q. Mu, Z. Gai, K. Hong and M. Zhang, "Paramagnetic Properties of Metal-Free Boron-Doped Graphene Quantum Dots and Their Application for Safe Magnetic Resonance Imaging", *Advanced Materials*, Vol. 29, No. 11, pp. 1–7, 2017.

40. Miura, K., Y. Egawa, T. Moriki, H. Mineta, H. Harada, S. Baba and S. Yamamoto, "Microscopic observation of chemical modification in sections using scanning acoustic microscopy", *Pathology International*, Vol. 65, No. 7, pp. 355–366, 2015.

41. Chong, Y., Y. Ma, H. Shen, X. Tu, X. Zhou, J. Xu, J. Dai, S. Fan and Z. Zhang, "The in vitro and in vivo toxicity of graphene quantum dots", *Biomaterials*, Vol. 35, No. 19, p. 5041–5048, 2014.

42. Saijo, Y., E. S. Filho, H. Sasaki, T. Yambe, M. Tanaka, N. Hozumi, K. Kobayashi and N. Okada, "Ultrasonic tissue characterization of atherosclerosis by a speed-of-sound microscanning system", *IEEE Transactions on Ultrasonics Ferroelectrics and Frequency Control*, Vol. 54, No. 8, pp. 1571–1577, 2007.

43. Akhtar, R., J. K. Cruickshank, X. Zhao, B. Derby and T. Weber, "A pilot study of scanning acoustic microscopy as a tool for measuring arterial stiffness in aortic biopsies", *Artery Research*, Vol. 13, pp. 1–5, 2016.

44. Saijo, Y., N. Hozumi, C. Lee, M. Nagao, K. Kobayashi, N. Oakada, N. Tanaka, E. S. Filho, H. Sasaki, M. Tanaka and T. Yambe, "Ultrasonic speed microscopy for imaging of coronary artery", *Ultrasonics*, Vol. 44, pp. 51–55, 2006.

45. Alivisatos, A. P., "Perspectives on the Physical Chemistry of Semiconductor Nanocrystals", *The Journal of Physical Chemistry A*, Vol. 100, pp. 13226–13239,

1996.

46. Rossetti, R., S. Nakahara and L. Brus, "Quantum size effects in the redox potentials, resonance Raman spectra, and electronic spectra of CdS crystallites in aqueous solution", *The Journal of Physical Chemistry A*, Vol. 79, No. 2, pp. 1086–1087, 1983.

47. Rossetti, R., S. Nakahara and L. Brus, "Size effects in the excited electronic states of small colloidal CdS crystallites", *The Journal of Physical Chemistry A*, Vol. 80, No. 9, pp. 4464–4469, 1984.

48. A.I.Ekimov, A.I.L.Efros and A.A.Onushchenko, "Quantum Size effect in semiconductor microcyrstals", *Solid State Communication*, Vol. 88, pp. 947–950, 1993.

49. Julie, A., Smydera and T. D. Krauss, "Coming attractions for semiconductor quantum dots", *Materials Today*, Vol. 14, No. 9, pp. 382–387, 2011.

50. Hines, M. A. and P. Guyot-Sionnest, "Synthesis and Characterization of Strongly Luminescing ZnS-Capped CdSe Nanocrystals", *The Journal of Physical Chemistry*, Vol. 100, pp. 468–471, 1996.

51. Ebenstein, Y., T. Mokari and B. U., "Fluorescence quantum yield of CdSe/ZnS nanocrystals investigated by correlated atomic-force and single-particle fluorescence microscopy", *Applied Physics Letter*, Vol. 80, pp. 4033– 4035, 2002.

52. Jr., M. B., M. Moronne, P. Gin, S. Weiss and A. P. Alivisatos, "Semiconductor Nanocrystals as Fluorescent Biological Labels", *Science*, Vol. 281, pp. 2013–2016, 1998.

53. Nida, D. L., N. Nitin, W. W. Yu, V. L. Colvin and R. Richards-Kortum, "Photostability of quantum dots with amphiphilic polymer-based passivation strategies", *Nanotechnology*, Vol. 219, 2008.

54. Bilen, B. T., M. Parlak and M. B. Unlu, "Scanning acoustic microscopy of quantum dot aggregates", *Biomedical Physics Engineering Express*, Vol. 5, No. 6, 2019.

55. Wang, B., E. Yantsen, T. Larson, A. B. Karpiouk, S. Sethuraman, J. L. Su, K. Sokolov, and S. Y. Emelianov, "Plasmonic Intravascular Photoacoustic Imaging for Detection of Macrophages in Atherosclerotic Plaques", *Nano Letters*, Vol. 9, No. 6, pp. 2212–2217, 2009.

56. Mantovani, A., G. Germano, F. Marchesi, M. Locatelli and S. K. Biswas, "Cancer-promoting tumor-associated macrophages: New vistas and open questions", *European Journal of Immunology*, Vol. 41, p. 2470–2525, 2011.

57. Jiang, S., Y. Yang, M. Fang, X. Li, X. Yuan and J. Yuan, "Co-evolution of tumor-associated macrophages and tumor neo-vessels during cervical cancer invasion", *Oncology Letters*, Vol. 12, pp. 2625–2631, 2016.

58. Peng, C. W., Q. Tian, G. F. Yang, M. Fang, Z. L. Zhang, J. Peng, Y. Li and D. W. Pang, "Quantum-dots based simultaneous detection of multiple biomarkers of tumor stromal features to predict clinical outcomes in gastric cancer", *Biomaterials*, Vol. 33, pp. 5742–5752, 2012.

59. Hatori, K., Y. Saijo, Y. Hagiwara, Y. Naganuma, K. I. K. M. Iikubo, K. Kobayashi and K. Sasaki, "Acoustic diagnosis device for dentistry", *Interface Oral Health Science*, Vol. 2016, pp. 181–201, 2016.

60. Chen, M., F. Cai, C. Wang, Z. Wang, L. Meng, F. Li, P. Zhang, X. Liu and H. Zheng, "Observation of Metal Nanoparticles for Acoustic Manipulation", *Advanced Science*, Vol. 4, pp. 1–9, 2017.

61. Wang, X., X. Sun, J. Lao, H. He, T. Cheng, M. Wang, S. Wang and F. Huang, "Multifunctional graphene quantum dots for simultaneous targeted cellular imaging and drug delivery", *Colloids and Surfaces B: Biointerfaces*, Vol. 122, pp.

638–644, 2014.

62. Shashkov, E. V., M. Everts, E. I. Galanzha and V. P. Zharov, "Quantum Dots as Multimodal Photoacoustic and Photothermal Contrast Agents", *Nano Letters*, Vol. 8, pp. 3953–3958, 2008.

63. Noh, M., T. Kim, H. Lee, C. Kim, S. Joo and K. Lee, "Fluorescence quenching caused by aggregation of water-soluble CdSe quantum dots", *Colloids and Surfaces A: Physicochemical and Engineering Aspects*, Vol. 359, pp. 39–44, 2010.

64. Qi, J., C. Sun, A. Zebibula, H. Zhang, R. T. K. Kwok, X. Zhao, W. Xi, J. W. Y. Lam, J. Qian and B. Z. Tang, "Real-Time and High-Resolution Bioimaging with Bright Aggregation-Induced Emission Dots in Short-Wave Infrared Region", *Advanced Materials*, Vol. 30, pp. 1–9, 2018.

65. Sheng, Z., B. Guo, D. Hu, S. Xu, W. Wu, W. H. Liew, K. Yao, J. Jiang, C. Liu, H. Zheng and B. Liu, "Bright Aggregation-Induced-Emission Dots for Targeted Synergetic NIR-II Fluorescence and NIR-I Photoacoustic Imaging of Orthotopic Brain Tumors", *Advanced Materials*, Vol. 30, pp. 1–8, 2018.

66. Qin, W., K. Li, G. Feng, M. Li, Z. yang, B. Liu and B. Z. Tang, "Bright and Photostable Organic Fluorescent Dots with Aggregation-Induced Emission Characteristics for Noninvasive Long-Term Cell Imaging", *Advanced Functional Materials*, Vol. 24, p. 635–643, 2014.

67. Fredricsson, B., L. Möller, [U+FFFD] Pousette and R. Westerholm, "Human sperm motility is affected by plasticizers and diesel particle extracts", *Pharmacology and Toxicology*, Vol. 72, pp. 128–133, 1993.

68. Sweeney, T., "Is exposure to endocrine distrupting compounds during fetal/postnatal development affecting the reproductive potential of farm animals?", *Domestic Animal Endocrinology*, Vol. 23, pp. 203–209, 2002.

69. Rusyn, I., J. M. Peters and M. L. Cunningham, "Modes of action and species-specific effects of di-(2-ethylhexyl)phthalate in the liver", *Critical Reviews in Toxicology*, Vol. 36, pp. 456–479, 2006.

70. Robinson, L. and R. Miller, "The impact of bisphenol a and phthalates on allergy, asthma, and immune function: a review of latest findings", *Current Environmental Health Reports*, Vol. 2, pp. 379 – 387, 2015.

71. Farquharson, S., C. Shende, F. E. Inscore, P. Maksymiuk and Gift, "A. Analysis of 5-fluorouracil in saliva using surface- enhanced raman spectroscopy.", *Journal of Raman Spectroscopy*, Vol. 36, p. 208–212, 2004.

72. Chan, J., D. S. Taylor, S. M. T. Z., Lane, K. Ihara and T. Huser, "Micro-raman spectroscopy detects individual neoplastic and normal hematopoietic cells", *Journal of Raman Spectroscopy*, Vol. 36, p. 208–212, 2006.

73. Notingher, I., C. Green and C. Dyer, "Discrimination between ricin and sulphur mustard toxicity in vitro using raman spectroscopy", *Journal of the Royal Society Interface*, Vol. 1, pp. 79–90, 2004.

74. W.T.Cheng, M.-T. L. and H. Liu, "Micro-raman spectroscopy used to identify and grade human skin pilomatrixoma", *Microscopy Research and Technique*, Vol. 68, pp. 75–79, 2004.

75. Frank, C. J., R. McCreecy and D.C.Bredd, "Raman spectroscopy of normal and diseased human breast tissues", *Analytical Chemistry*, Vol. 67, pp. 777– 783, 1995.

76. Huang, Z., D. McLean and H. Zeng, "Raman spectroscopy in combination with background near- infrared auto-fluorescence enhances the in vivo assessment of malignant tissues", *Photochemistry and Photobiology*, Vol. 81, p. 1219–1226, 2005.

77. Ruiz-Chica, M. A., F. M., Sanchez-Jimenez and F. Ramirez, "Characterization by raman spectroscopy of conformational changes on guanine–cytosine and ade-

nine–thymine oligonucleotides induced by aminooxy analogues of spermidine.", *Journal of Raman Spectroscopy*, Vol. 35, p. 93–100, 2004.

78. Gniadecka, M., H. Wulf and D. Nielsen, "Diagnosis of basal cell carcinoma by raman spectroscopy.", *Journal of Raman Spectroscopy*, Vol. 28, p. 125–129, 1997.

79. Dukor, R., "Vibrational spectroscopy in the detection of cancer", *Biomedical applications*, Vol. 5, p. 3335–3359, 2002.

80. E.B. Hanlon, a. R. M. e. a., "Prospects for in vivo raman spectroscopy", *Physics in Medicine and Biology*, Vol. 45, pp. 1–59, 2000.

81. Malini, R., K. Venkatakrishna, J. Kurien, K. M. Pai, V. B. K., L. Rao and C. M. Krishna, "Discrimination of normal, inflammatory, premalignant, and malignant oral tissue: A raman spectroscopy study.", *Biopolymers*, Vol. 81, p. 179–193, 2006.

82. Stone, N., C. Kendall, P. J. S. Crow and H. Barr, "Raman spectroscopy for identification of epithelial cancers", *Faraday Discussions*, Vol. 126, pp. 141–157, 2004.

83. Krafft, C., T. Simat and R. Salzer, "Near infrared raman spectra of human brain lipids", *Spectrochimica Acta*, Vol. 61, pp. 1529–1535, 2004.

84. Stone, N., N. C. K., Shepherd, P. Crow and H. Barr, "Near-infrared raman spectroscopy for the classification of epithelial pre-cancers and cancers", *Journal of Raman Spectroscopy*, Vol. 33, p. 564–573, 2002.

85. Agarwal, R., V. G. and P. Tandon., "Phonon dispersion in poly(di-methylsilane", *Journal of Organometallic Chemistry*, Vol. 691, p. 2902–2908, 2006.

86. Sedha, S., S. Kumar and S. Shukla, "Role of oxidative stress in male reproductive dysfunctions with reference to phthalate compounds", *Urology Journal*, Vol.

12(5), p. 2304–2316, 2015.

87. Asghari, M. H., S. Saeidnia and M. Abdollahi, "A review on the biochemical and molecular mechanisms of phthalate-induced toxicity in various organs with a focus on the reproductive system", *International Journal of Pharmacology*, Vol. 11(2), p. 95–105, 2015.

88. Sobarzo, C. M., M. R. Nde, L. Livia, D. Berta and H. F. N. Schteingart, "Mono-(2-ethylhexyl) phthalate (MEHP) affects intercellular junctions of sertoli cell: A potential role of oxidative stress", *Reproductive Toxicology*, Vol. 58, p. 203–212, 2015.

89. Cho, Y. J., S. B. Park and M. N. Han, "Di-(2-ethylhexyl)-phthalate induces oxidative stress in human endometrial stromal cells in vitro", *Molecular and Cellular Endocrinology*, Vol. 407, pp. 9–17, 2015.

90. Tetz, L. M. e. a., "Mono-2-ethylhexyl phthalate induces oxidative stress responses in human placental cells in vitro", *Toxicology and Applied Pharmacology*, Vol. 268, No. 1, pp. 47–54, 2013.

91. Prasanth, G. K., L. M. Divya and C. N. Sadasivan, "Effects of mono and di(nbutyl) phthalate on superoxide dismutase", *Toxicology*, Vol. 262, No. 1, p. 38–4, 2009.

92. Garberg, P. and J. Hogberg, "Selenium metabolism in isolated hepatocytes: inhibition of incorporation in proteins by mono(2-ethylhexyl)phthalate, a metabolite of the peroxisome proliferator di(2-ethylhexyl)phthalate", *Carcinogenesis*, Vol. 12, pp. 7–12, 1991.

93. Aydemir, D. e. a., "Impact of the di(2-ethylhexyl) phthalate administration on trace element and mineral levels in relation of kidney and liver damage in rats.", *Biological Trace Element Research*, Vol. 186, No. 2, p. 474–488, 2018.

94. Erkekoglu, P. e. a., "Induction of ROS, p53, p21 in DEHP- and MEHP exposed LNCaP cells-protection by selenium compounds", *Food and Chemical Toxicology*, Vol. 49, No. 7, p. 1565–1571, 2011.

95. Aydemir, D., G. Karabulut, M. Gok, N. Barlas and N. N. Ulusu, "Data the DEHP induced changes on the trace element and mineral levels in the brain and testis tissues of rats", *Data Brief*, Vol. 26, 2019.

96. Lindgren, A., Lindquist, L. N. G., T. A., Olsson and S. Ullberg, "A whole body autoradiographic study on the distribution of 14C-labelled di-(2- ethylhexyl)phthalate in mice", *Toxicology*, Vol. 23, p. 149–158, 1982.

97. Dong, J., A. C. Drohat, J. T. Stivers, P. K. W. and P. R. Carey, "Raman spectroscopy of uracil dna glycosylase- dna complexes: Insights into dna damage recognition and catalysis", *Biochemistry*, Vol. 39, p. 13241–13250, 2000.

98. Panikkanvalappil, M. S. R., M. M. A., M. A. and M. A. El-Sayed, "Surface-enhanced raman spectroscopy for real-time monitoring of reactive oxygen species-induced dna damage and its prevention by platinum nanoparticless", *ACS nano*, Vol. 7, p. 7524–7533, 2013.

99. Hauser, R. e. a., "Dna damage in human sperm is related to urinary levels of phthalate monoester and oxidative metabolites", *Human Reproduction*, Vol. 22, p. 688–695, 2007.

100. Mann, A. H. e. a., "Comparison of the short-term effects of di (2-ethylhexyl) phthalate, di (n-hexyl) phthalate, and di (n-octyl) phthalate in rat", *Toxicology and Applied Pharmacology*, Vol. 77, p. 116–132, 1985.

101. Ganning, A. E., U. Brunk and G. Dallner, "Phthalate esters and their effect on the liver", *Hepatology*, Vol. 4, p. 541–547, 1984.